Published in final edited form as:

Sci Transl Med. 2021 July 28; 13(604): . doi:10.1126/scitranslmed.abc8922.

Blockade of the CD93 pathway normalizes tumor vasculature to facilitate drug delivery and immunotherapy

Yi Sun[1], **Wei Chen**[1,2], **Robert J. Torphy**[1], **Sheng Yao**[3], **Gefeng Zhu**[3], **Ronggui Lin**[1], **Roberta Lugano**[4], **Emily N. Miller**[1], **Yuki Fujiwara**[1], **Li Bian**[5], **Linghua Zheng**[3], **Sudarshan Anand**[6], **Fan Gao**[7], **Weizhou Zhang**[8], **Sarah E. Ferrara**[9], **Andrew E. Goodspeed**[9,10], **Anna Dimberg**[4], **Xiao-Jing Wang**[5,11], **Barish H. Edil**[12], **Carlton C. Barnett**[1], **Richard D. Schulick**[1], **Lieping Chen**[3,*], **Yuwen Zhu**[1,*]

[1]Department of Surgery, University of Colorado Anschutz Medical Campus, Aurora, CO 80045, USA.

[2]Cancer Institute of Integrated Traditional Chinese and Western Medicine, Zhejiang Academy of Traditional Chinese Medicine, Hangzhou, Zhejiang 310012, P. R. China.

[3]Department of Immunobiology, Yale University School of Medicine, New Haven, CT 06520, USA.

[4]Department of Immunology, Genetics and Pathology, Science for Life Laboratory, Rudbeck Laboratory, Uppsala University, 75185 Uppsala, Sweden.

[5]Department of Pathology, University of Colorado Anschutz Medical Campus, Aurora, CO 80045, USA.

[6]Department of Cell, Development and Cancer Biology, Oregon Health and Science University, Portland, OR 97239, USA.

[7]Caltech Bioinformatics Resource Center at Beckman Institute, California Institute of Technology, Pasadena, CA 91125, USA.

[8]Department of Pathology, University of Florida, Gainesville, FL 32610, USA.

[9]University of Colorado Comprehensive Cancer Center, Aurora, CO 80045, USA.

[10]Department of Pharmacology, University of Colorado Anschutz Medical Campus, Aurora, CO 80045, USA.

---

[*]Corresponding author. yuwen.zhu@cuanschutz.edu (Y.Z.); lieping.chen@yale.edu (L.C.).

Author contributions: Y.S., L.C., and Y.Z. conceived the project, designed experiments, and wrote the manuscript. Y.S., W.C., R.J.T., S.Y., G.Z., R. Lin, R. Lugano, E.N.M., Y.F., L.B., and L.Z. performed experiments and collected data. Y.S., F.G., S.E.F., and A.E.G. analyzed bioinformatics data. S.A., W.Z., A.D., X.-J.W., B.H.E., C.C.B., and R.D.S. provided resources and critical comments of the manuscript. R.D.S., L.C., and Y.Z. supervised the project.

SUPPLEMENTARY MATERIALS

stm.sciencemag.org/cgi/content/full/13/604/eabc8922/DC1

Materials and methods

Figs. S1 to S10

Table S1

Data file S1

[11]Veterans Affairs Medical Center, VA Eastern Colorado Health Care System, Aurora, CO 80045, USA.

[12]Department of Surgery, University of Oklahoma Health Sciences Center, Oklahoma City, OK 73104, USA.

Abstract

The immature and dysfunctional vascular network within solid tumors poses a substantial obstacle to immunotherapy because it creates a hypoxic tumor microenvironment that actively limits immune cell infiltration. The molecular basis underpinning this vascular dysfunction is not fully understood. Using genome-scale receptor array technology, we showed here that insulin-like growth factor binding protein 7 (IGFBP7) interacts with its receptor CD93, and we subsequently demonstrated that this interaction contributes to abnormal tumor vasculature. Both CD93 and IGFBP7 were up-regulated in tumor-associated endothelial cells. IGFBP7 interacted with CD93 via a domain different from multimerin-2, the known ligand for CD93. In two mouse tumor models, blockade of the CD93/IGFBP7 interaction by monoclonal antibodies promoted vascular maturation to reduce leakage, leading to reduced tumor hypoxia and increased tumor perfusion. CD93 blockade in mice increased drug delivery, resulting in an improved antitumor response to gemcitabine or fluorouracil. Blockade of the CD93 pathway triggered a substantial increase in intratumoral effector T cells, thereby sensitizing mouse tumors to immune checkpoint therapy. Last, analysis of samples from patients with cancer under anti–programmed death 1/ programmed death-ligand 1 treatment revealed that overexpression of the IGFBP7/CD93 pathway was associated with poor response to therapy. Thus, our study identified a molecular interaction involved in tumor vascular dysfunction and revealed an approach to promote a favorable tumor microenvironment for therapeutic intervention.

INTRODUCTION

Abnormal vasculature is a key pathological feature facilitating tumor outgrowth and metastasis (1, 2). Although normal vascular angiogenesis is required to support tissue homeostasis, the formation of structurally altered blood vessels in tumors often leads to tumor hypoxia, low pH, and decreased drug penetration into the tumor microenvironment (TME) (3, 4). Abnormal tumor vasculature poses a substantial obstacle to immunotherapy as it actively limits effector T cell infiltration into the TME by down-regulating adhesion molecules including intercellular adhesion molecule 1(ICAM1) and vascular cell adhesion molecule 1 (VCAM1) and by increasing the expression of inhibitory molecules such as programmed death-ligand 1 (PD-L1) [also known as B7 homolog 1 (B7-H1)] and Fas ligand (5). Hypoxia and subsequently reprogrammed energy metabolism within tumors limit the survival and effector functions of CD8$^+$ T cells (6). In addition, hypoxia and low pH in the TME may promote regulatory T cell (T$_{reg}$) development and recruitment and drive tumor-associated macrophages to their suppressive form (7, 8). Therefore, targeting the tumor vasculature represents a major effort for the development of cancer therapy.

The vascular endothelial growth factor (VEGF) family represents one of the most well-validated signaling pathways in tumor angiogenesis (9). In addition to driving angiogenesis, excessive VEGF promotes permeability in vasculature and leads to chaotic, leaky blood vessels in tumors (10). VEGF inhibitors, including monoclonal antibodies (mAbs) or targeting small molecules, were believed to suppress tumor angiogenesis, but several studies have also shown that low doses of anti–VEGF receptor (VEGFR) therapy can normalize immature, leaky tumor blood vessels (11, 12). Distinct from the inhibition of angiogenesis, vascular normalization promotes the formation of a functional vascular network in tumors, reverses hypoxia and increases vascular perfusion (13, 14), and enhances immune cell infiltration within tumors (15). A positive feedback loop between vascular normalization and T cell–mediated immunotherapy exists, as interferon-γ (IFN-γ) produced by intratumoral T cells increases the expression of adhesion molecules on the endothelium for immune cell infiltration (16). VEGF blockade improves the efficacy of immunotherapy including vaccines, anti–programmed death 1 (PD1)/PD-L1 mAb therapy (anti-PD therapy), and adaptive cellular therapy (17) in a variety of preclinical tumor models. Improved clinical outcomes have been observed using a combination of VEGF inhibitors and anti-PD therapy in several cancer types, including endometrial cancer (18), renal cell cancer (19), non–small cell lung cancer (20), ovarian cancer (21), and hepatocellular carcinoma (22).

Because VEGF signaling is essential for normal tissue vascular angiogenesis, VEGF inhibitors in cancer therapy is often associated with hypertension and nephrotoxicity (23, 24). We reasoned that excessive VEGF signaling in tumors activates distinct downstream pathways to promote vascular abnormalities. If this is the case, then it would be beneficial to identify pathways underlying tumor vascular abnormalities, which may not be essential for normal tissue vessel homeostasis (25). Here, we compared gene expression profiles in tumors under the treatment of VEGF inhibitors (26–28). We identified CD93 as a candidate receptor that was down-regulated in the setting of VEGF inhibition and a potential target that mediates vascular normalization. CD93—a C-type lectin transmembrane protein primarily expressed in endothelial cells (ECs), immature B cells, and monocytes—has been widely reported to play important roles in vascular angiogenesis (29–31). Using a genome-scale receptor array system (GSRA) (32), we identified insulin-like growth factor binding protein 7 (IGFBP7), an extracellular matrix (ECM) protein on tumor vasculature, as a ligand for CD93. These findings permitted further exploration of the mechanisms of action and manipulation of this pathway to improve cancer therapy.

RESULTS

CD93 on tumor vasculature is up-regulated by VEGF

To identify new targets that could be responsible for VEGF inhibitor– induced vascular normalization, we studied gene expression profiles in tumors under the treatment of VEGF inhibitors in vivo from four recently published gene expression datasets (26–28). Among them, three databases were from human tumor xenograft models, whereas the fourth was from a transgenic mouse model of pancreatic neuroendocrine tumors (PNETs) (table S1). We identified genes that were consistently reduced across multiple datasets with a cutoff $\log_2$ fold change < -0.5. We identified 11 genes whose expressions were greatly reduced by VEGF inhibitors in at least three datasets (fig. S1A). We selected five candidate genes known to be up-regulated in tumor ECs and tested their roles in angiogenesis using a tube formation assay with human umbilical vein ECs (HUVECs). Among them, knockdown of *CD93* genes led to the greatest reduction in tube formation (fig. S1B), confirming a proangiogenetic role for CD93 in ECs.

CD93 is one of the top genes in a previously reported human primary tumor angiogenesis gene signature (26), and CD93 overexpression in tumor vasculatures has been observed in many solid tumors (29, 33). Immunohistochemistry staining indicated that CD93 protein was up-regulated in pancreatic adenocarcinoma (PDA) and PNET, the two main tumor types in the pancreas (fig. S1C). Immunofluorescent (IF) staining of human kidney cancer, head and neck cancer, and colon cancer revealed that CD93 was mainly expressed in tumor vasculature (fig. S1D). Supporting that, analysis of published single-cell RNA sequencing (scRNA-seq) datasets of multiple human tumor tissues revealed that ECs are the primary cell type expressing CD93 (fig. S1E).

We also evaluated CD93 expression in mouse normal tissues and tumors. Surface CD93 in mouse aortic ECs (MAECs) was negligible, but its expression could be up-regulated by incubation with mouse VEGF-A, confirming that VEGF signaling directly regulates CD93 expression (fig. S1F). In normal mouse pancreas and skin, blood vessels express very low CD93; CD93 in tumor vasculature was substantially increased in an orthotopic murine PDA model, using a mouse tumor line derived from the *LSL-Kras*$^{G12D/+}$; *LSL-Trp53*$^{R172H/+}$; *Pdx-1-Cre* (KPC) mice (34), and in a subcutaneous B16 melanoma model (fig. S1, G and H). Together, our results indicate that CD93 is selectively up-regulated in tumor vasculature that may be due to VEGF exposure in the TME.

CD93 antibody normalizes tumor vasculature and suppresses tumor growth in mice

To evaluate the possible effect of CD93 in vivo, we generated a mAb [clone 7C10, rat immunoglobulin G (IgG)] against mouse CD93 (mCD93) by immunizing a rat with mouse CD93 fusion protein. The specificity of 7C10 was validated by its specific interaction with mCD93-expressing human embryonic kidney (HEK) 293T cells (fig. S2A), with affinity measured at dissociation constant (K_d) = 2.524 × 10^{-10} M (fig. S2B). 7C10 stained CD11b$^+$ monocytes in peripheral blood from wild-type (WT) but not CD93$^{-/-}$ mice (fig. S2C). When the antibody was intraperitoneally injected into mice with established B16 tumors, 7C10 strongly stained tumor vasculature of WT but not CD93$^{-/-}$ mice (fig. S2D), further supporting its specific binding to mCD93.

When we administrated this CD93 mAb into WT B6 mice implanted with KPC tumor cells, 7C10 alone was able to reduce KPC tumor growth by about 60% (Fig. 1A). Treatment with anti-CD93 mAb also inhibited the progression of subcutaneous B16 melanoma in mice (Fig. 1B). IF staining of KPC tumor tissues did not show a clear change in CD31$^+$ vessel density upon anti-CD93 treatment (Fig. 1C). Pericytes and vascular smooth muscle cells supporting the endothelial layer of blood vessels play key roles in blood vessel maturation and function (35, 36). Upon anti-CD93 treatment, there was an about fourfold increase in the percentage of pericyte-covered blood vessels, based on costaining of neural/glial antigen 2 (NG2) and CD31, compared to control tumors (Fig. 1D). In line with this observation, there were about four times as many blood vessels with α–smooth muscle actin (αSMA)–positive staining within 7C10-treated tumors (Fig. 1E). We isolated tumor

ECs and performed RNA-seq to investigate genome-wide expression changes in response to the treatment of anti-CD93. Many of the genes affected by anti-CD93 were functionally related to cell adhesion, angiogenesis or vasculature development, including *bcl-2 and 19-kDa interacting protein-3* (*BNIP3*) (37), *MAF bZIP transcription factor A* (*MAFA*) (38), *hydroxymethylglutaryl* (*HMG*)*–CoA synthase 2* (*HMGCS2*) (39), *aldehyde dehydrogenase 1 family member A3* (*ALDH1A3*) (40), *secreted frizzle-related protein 2* (*SFRP2*) (41), and *GATA binding protein 1* (*GATA1*) (Fig. 1F) (42). Gene Ontology analysis confirmed that the transcriptomic changes by anti-CD93 treatment were mainly related to biological pathways of angiogenesis, cell adhesion, or vasculature development (Fig. 1G). We validated changes in gene expression by quantitative polymerase chain reaction (qPCR) (Fig. 1, H and I). The up-regulations of BNIP3, ALDH1A3, and MAFA proteins in tumor vasculature by anti-CD93 were able to be further confirmed by IF staining (fig. S3A).

Next, we examined whether the structural changes in tumor vasculature in response to CD93 blockade could translate into functional improvements. The KPC tumor-bearing mice mentioned above underwent 1 week of antibody treatment before receiving intravenous injection of fluorescein isothiocyanate–lectin (FITC-lectin) or FITC-dextran. We found that in control (untreated) tumors, only a few blood vessels located at the edge of the tumors were FITC positive, whereas in tumors treated with 7C10, most vessels in both the center and at the edge of the tumor were stained with FITC-lectin. Overall, there were more than threefold more perfused blood vessels (FITC-lectin positive) in 7C10-treated tumors than in the control (Fig. 1J). Consistently, anti-CD93 treatment reduced the leakage area (dextran positive) of tumors by about 50% (Fig. 1K). Treatment with anti-CD93 also improved tumor vascular maturation and increased blood perfusion in B16 melanoma mice (fig. S3, B and C).

CD93 is also expressed on several immune cell types, including monocytes, immature B cells, and platelets (43). To further support that the CD93 mAb targets blood vessels, we constructed CD93 chimeric mice by reconstituting lethally irradiated WT B6 mice with bone marrow (BM) cells from CD93$^{-/-}$ mice. When we inoculated chimeric mice with B16 tumors, tumor growth was similar between mice reconstituted with CD93$^{-/-}$ BM cells and control mice reconstituted with WT BM cells, implying a nonessential role of hematopoietic CD93 on antitumor response. Treatment with CD93 mAb inhibited tumor growth in both mice to a similar extent, further supporting that anti-CD93 likely works to target CD93 on tumor vasculature (Fig. 1L).

We attempted to exclude the possible impact of reduced tumor size by anti-CD93 on tumor perfusion and hypoxia. We injected FITC-lectin and pimonidazole to compare tumor vasculature between control tumors implanted for 6 and 10 days and CD93 mAb–treated tumors implanted for 10 days. Tumor sizes were comparable between the 6-day control group (control D6) and the 10-day anti-CD93 group (anti-CD93 D10). Only about 25 to 30% of tumor vasculature in control groups stained for FITC-lectin, whereas more than 60% of blood vessels in anti-CD93–treated tumors were FITC-lectin–positive (fig. S3D); consistently, anti-CD93 treatment reduced tumor hypoxia from 20% pimonidazole staining in control groups to 10% in anti-CD93–treated tumors (fig. S3D).

We compared the vascular effects between the anti-CD93 and VEGFR2 mAb (clone DC101), a mAb commonly used to block VEGF signaling in mice (11). In the KPC tumor murine model, CD93 and VEGFR2 antibodies exhibited comparable antitumor activity (fig. S4A). Both antibodies led to tumor vascular maturation, whereas only the treatment of VEGFR2 mAb displayed anti-angiogenetic effect to markedly reduce blood vessels within tumors (fig. S4B). We further treated naive healthy mice with antibodies to evaluate for potential vascular changes in healthy tissues. The treatment of anti-CD93 revealed no clear effect on tissue blood vessels; however, a similar treatment with anti-VEGFR2 systemically inhibited normal vascular homeostasis in many healthy tissues and organs (fig. S4C), which is consistent with a previous report (44). In a skin wound healing mouse model, CD93 mAb did not interfere with vascular angiogenesis to slow down wound healing, which was in sharp contrast to anti-VEGFR2 (fig. S4, D to F). These results support that targeting CD93 by mAb in vivo have a minor anti-angiogennic effect compared to anti-VEGF/VEGFR drugs.

IGFBP7 is a ligand for CD93

To facilitate our research into CD93, a GSRA system was used to search for a counter-receptor to CD93. The GSRA is a high-throughput gene expression system with the capacity to display thousands of transmembrane and secreted proteins to study protein-protein interactions (32). IGFBP7, a secreted protein of the IGFBP family, was the only positive hit out of ~6600 human transmembrane and secreted proteins in the library (Fig. 2A). We confirmed their specific interaction by flow cytometry; as expected, the addition of a human CD93 mAb or IGFBP7 mAb markedly reduced the binding of IGFBP7 protein to CD93-transfected HEK293T cells (Fig. 2B). Recombinant IGFBP7 protein bound HUVEC cells positively and the CD93 mAb completely eliminated this binding activity (Fig. 2C), demonstrating that CD93 mediates the binding of IGFBP7 to HUVEC cells. Affinity measurement of the IGFBP7/CD93 interaction by microscale thermophoresis (MST) showed a K_d value at 53.13 ± 20.19 nM (Fig. 2D). When we screened a library containing about 5600 transmembrane proteins with IGFBP7 protein, CD93 was the only identified binding partner for IGFBP7, further demonstrating the specific interaction between CD93 and IGFBP7 (fig. S5, A and B). Human and mouse CD93 proteins share about 70% amino acid sequence identity, whereas IGFBP7 protein is relatively more conserved (90% amino acid sequence identity between human and mouse). The interaction between CD93 and IGFBP7 was conserved in mouse, and this binding could be blocked by an anti-mouse IGFBP7 mAb (clone 2C6) or an anti-mouse CD93 mAb (clone 7C10) (Fig. 2E), which we used in the in vivo studies mentioned above. Thus, our results suggest that CD93 mAb 7C10 executes its effect in the tumor vasculature by blocking the IGFBP7/CD93 interaction.

IGFBP7 and multimerin-2 interact with different domains of CD93

In addition to IGFBP7, multimerin-2 (MMRN2), an ECM protein that happens to be absent in our GSRA library (32), is another known ligand for CD93 (45, 46). Unlike MMRN2 that binds multiple members of the group 14 C-type lectin family, IGFBP7 interacted with CD93 only (fig. S5C). Knockdown of IGFBP7 in HUVEC cells did not reduce surface CD93 expression (fig. S5D), which is different from MMRN2, whose interaction stabilizes cell surface CD93 by protecting it from cleavage (31). MMRN2 and IGFBP7 did not compete for CD93 binding, because the addition of IGFBP7 did not interfere with the CD93 binding by MMRN2 (Fig. 2F) and vice versa (Fig. 2G). In an enzyme-linked immunosorbent assay (ELISA) assay, the preincubation of CD93 protein in IGFBP7-coated wells led to the binding of MMRN2 (Fig. 2H), suggesting that CD93 can bind to its two ligands to form a complex together. When we examined the binding of these two ligands to mouse CD93 proteins with various point mutations, two mutants within the long loop region of the C-type lectin-like domain (CTLD) of CD93 (C103S and C135S) lost binding to MMRN2 (45) but still bound to IGFBP7 (fig. S5E). To specify the binding site on CD93 for IGFBP7 binding, we generated two chimeric proteins by exchanging the CTLD domain between CD93 and CD141; both chimeric molecules minimally interacted with IGFBP7, suggesting that both the CTLD domain and the non-CTLD fragment of CD93 are required for IGFBP7 interaction (fig. S5F). We made several truncated CD93 proteins to further determine the binding site for IGFBP7; as shown in Fig. 2I, IGFBP7 binding to CD93 required the first two epidermal growth factor (EGF)–like domains. Our mouse CD93 antibody 7C10 happened to bind the CTLD domain of CD93 (Fig. 2I) and was able to block the CD93 binding by MMRN2 (Fig. 2J).

IGFBP7 contains an IGF-binding (IB) domain at its N terminus, a Kazal-type serine proteinase inhibitor domain (Kazal) in its central region, and an Ig-like C2-type (IgC2) domain at its C terminus (47). To investigate the binding interaction between IGFBP7 and CD93, we generated a series of chimeric proteins by replacing each domain of IGFBP7 with a corresponding portion from IGFBPL1 (48), an IGFBP-related protein that does not bind CD93. Chimeric IGFBP7 proteins with the replacement of the IB domain lost the ability to bind CD93$^+$ 293T cells, whereas replacement of the Kazal or IgC2 domain had either minimal or no effect (Fig. 2K). These results demonstrated that the IB domain of IGFBP7 mediates the interaction to CD93. No IB-containing human proteins other than IGFBP7 could interact with CD93 (fig. S5G). Therefore, the IB domain of IGFBP7 is specific for the interaction with CD93.

IGFBP7 expression in tumor vasculature can be induced by hypoxia and VEGF

We analyzed IGFBP7 expression in tissue samples from patients with PDA by IF staining. In adjacent normal pancreas tissues, few blood vessels had detectable IGFBP7 protein; CD31 staining was scarce in human PDA tissues. However, there were over twice as many blood vessels that were IGFBP7 positive in PDA compared to adjacent normal pancreas (Fig. 3A). Likewise, analysis of The Cancer Genome Atlas (TCGA) and the Genotype-Tissue Expression (GTEx) datasets revealed that *IGFBP7* transcription was greatly up-regulated in human PDA (fig. S6A). *IGFBP7* gene expression in PDA correlated well with EC signature genes, supporting *IGFBP7* as a gene enriched in tumor-associated ECs (fig. S6B). Meta-analysis of an online endothelial cell database (EndoDB) (https://endotheliomics.shinyapps.io/endodb/) further supported that *IGFBP7* is up-regulated in tumor-associated ECs (fig. S6C). IGFBP7 protein was barely detectible in blood vessels of normal human tissues; however, its expression in the vasculatures of tumor tissues was markedly up-regulated (fig. S6D). As exemplified in a head and neck cancer tissue (Fig. 3B), IGFBP7 was strongly expressed on blood vessels within the tumor tissue, but not those vessels adjacent to the tumor. In mouse tumor tissues, including orthotopically implanted

KPC tumors and subcutaneous B16 tumors, we observed up-regulation of IGFBP7 in the tumor vasculature (fig. S6E). Thus, our results support that IGFBP7 is up-regulated in the tumor vasculature.

Blood vessels within the center of implanted mouse KPC tumors expressed higher concentrations of IGFBP7 compared to those around the edge of the tumor (fig. S6F), and blood vessels within hypoxia-inducible factor-1α (HIF-1α)–positive tumor areas tended to express higher concentrations of IGFBP7 (fig. S6G). These implied that IGFBP7 up-regulation could be caused by hypoxia within the tumor. We therefore cultured ECs in dimethyloxalylglycine (DMOG) to mimic hypoxic conditions. We found that HUVEC cells cultured in DMOG increased HIF-1α and had higher IGFBP7 protein expression (Fig. 3C). The *IGFBP7* gene does not have a clear hypoxia response element (49) in the promoter region. We reasoned that hypoxia-induced VEGF, a strong inducer of IGFBP7 in ECs (50), could be responsible for IGFBP7 up-regulation. Inclusion of a mouse VEGFR2-blocking mAb completely prevented DMOG-induced IGFBP7 expression in mouse ECs (Fig. 3D). Analysis of the scRNA-seq data (GSE110501) from a xenograft colon cancer mouse model (51) revealed that *IGFBP7* transcription was inhibited in tumor ECs by aflibercept, a VEGF inhibitor (fig. S6H). Together, our results support that IGFBP7 is a hypoxia-induced ECM protein in tumor vasculature that may be up-regulated by VEGF signaling.

IGFBP7 promotes EC angiogenesis via CD93

IGFBP7, also known as angiomodulin or MAC25, has been shown to promote EC angiogenesis (50, 52). The knockdown of *IGFBP7* gene expression inhibited tube formation in HUVEC cells (fig. S7A). We transfected HUVEC cells with CD93 small interfering RNA to knockdown CD93 as an in vitro model to test the effect of IGFBP7. As expected, the addition of exogenous IGFBP7 protein increased WT HUVEC cell tube formation and migration. However, in the CD93-knockdown HUVEC cells, IGFBP7 protein lost its ability to promote tube formation (fig. S7B) and EC migration (fig. S7C). Thus, our studies indicate that CD93 mediates the proangiogenic effect of IGFBP7 on ECs.

To test the effect of IGFBP7 on tumor growth and tumor vasculature in vivo, we used a mouse IGFBP7 mAb (clone 2C6), which blocks the binding of IGFBP7 to CD93 (Fig. 2E and fig. S7, D and E). Administration of anti-IGFBP7 inhibited murine KPC tumor growth by more than 40% relative to the control (fig. S7F). The same IGFBP7 mAb did not further improve antitumor response by anti-CD93 (fig. S7G), suggesting that the IGFBP7 and CD93 antibodies might target the same pathway. IF staining of tumor tissues revealed that IGFBP7 blockade did not affect the density of $CD31^+$ blood vessels (fig. S7H). Similar to the CD93 mAb, anti-IGFBP7 improved $NG2^+$ pericyte coverage of blood vessels (fig. S7I) and increased αSMA-positive blood vessels within tumors (fig. S7J). Treatment with anti-IGFBP7 increased platelet-derived growth factor receptor β $(PDGFR\beta)^+$ pericyte coverage on tumor vessels (fig. S7K) while reducing angiopoietin-2 (Ang2)–positive vessels (fig. S7L), which were commonly observed in studies of vascular maturation (14, 53, 54). Integrin β1 activation leads to EC destabilization and is involved in Ang2-triggered vascular permeability (55) and CD93-mediated fibronectin fibrillogenesis (31). Tumor tissues from mice treated with 2C6 mAb displayed a reduction of β1 integrin activation by more than

50% (fig. S7M), further supporting that anti-IGFBP7 affects CD93-mediated signaling to normalize tumor vasculature. Our results support that blockade of the IGFBP7/CD93 interaction promotes vascular maturation and attenuates tumor growth.

Blockade of the CD93 pathway improves chemotherapy

We then tested whether blockade of the CD93 pathway could promote drug delivery as a result of vascular normalization. In the KPC mouse model, we tested the delivery of doxorubicin, an anthracycline chemotherapeutic with intrinsic fluorescence (29), after treatment with anti-CD93. Mice were intravenously injected with doxorubicin 20 min before sacrificing; at the same time, mice were administrated with pimonidazole to evaluate tumor hypoxia. Greater penetration of doxorubicin into tumors was observed in CD93 mAb–treated mice; in conjunction, hypoxia in tumors was reduced by anti-CD93 (Fig. 4A). In addition to increased drug delivery, treatment with anti-CD93 improved the antitumor efficacy of gemcitabine in KPC tumors (Fig. 4, B and C), as demonstrated by analyzing tumor cell proliferation and apoptosis based on Ki-67 and cleaved caspase 3 (CC3) staining, respectively (Fig. 4D). In the B16 tumor mouse model, the combination of 5-fluorouracil (5-FU) and CD93 mAb was able to substantially inhibit tumor growth (Fig. 4E) and extend the survival of mice (Fig. 4F). CD93 blockade also enhanced 5-FU–induced suppression of B16 tumor proliferation and 5-FU–triggered tumor apoptosis (Fig. 4G). Together, our experiments demonstrate that CD93 blockade reduces hypoxia and promotes drug delivery.

CD93 blockade increases immune cell infiltration to inhibit tumor progression

Normalization of tumor vasculature enhances immune cell trafficking into the tumors, which may be due to up-regulated adhesion molecules (11, 14, 56). Anti-CD93 treatment increased ICAM1 expression on tumor blood vessels in subcutaneous KPC and B16 murine tumor models (fig. S8, A and B). IF staining of the KPC tumors revealed that anti-CD93 triggered a two- to threefold increase of $CD3^+$ T cells compared to untreated mice on days 8 and 15 (Fig. 5, A and B); both $CD4^+$ and $CD8^+$ T cells were increased within tumors treated with anti-CD93 (fig. S8C). Treatment with IGFBP7 blocking mAb (2C6) also exhibited an increase in intratumoral $CD3^+$ T cells in KPC tumors (fig. S8D). Flow cytometry analysis of immune cell compositions revealed that anti-CD93 substantially increased the percentage and density of $CD45^+$ leukocytes in tumors (Fig. 5, C and D). Detailed cell type analysis indicated that both $CD4^+$ and $CD8^+$ T cell subsets, as well as natural killer (NK) and NK T (NKT) cells, were increased in CD93 mAb–treated tumors (Fig. 5D); in contrast, the densities of myeloid-derived suppressor cells (MDSCs) within tumors, including both granulocytic MDSCs (gMDSCs) and monocytic MDSCs, were reduced by anti-CD93 (Fig. 5D). The $CD3^+$ T cell compartment, particularly $CD8^+$ T cells, was proportionally increased in CD93 mAb–treated tumors (fig. S8E); consistently, anti-CD93 increased proportions of IFN-γ^+ and tumor necrosis factor–α^+ (TNF-α^+) $CD8^+$ T cells within tumors (Fig. 5E). Although anti-CD93 did not alter the percentage of the $CD4^+$ T cells within the $CD45^+$ cell compartments (fig. S8E), the treatment of anti-CD93 reduced the proportion of $Foxp3^+$ T_{reg} cells in $CD4^+$ T cells (Fig. 5F). Concurrently, anti-CD93 increased high endothelial venule (HEV)–like structures within the tumor (Fig. 5G), which could contribute to increased intratumoral T cells by vascular normalization (57). We observed a similar effect of anti-CD93 on promoting $CD3^+$ T cell infiltration in B16 melanoma (Fig. 5H). The vascular effect of anti-CD93 on increased T cell infiltration was further supported by the tumor study in CD93 chimeric mice in which B16 tumors in WT mice reconstituted with $CD93^{-/-}$ BM cells were still responsive to the treatment of anti-CD93 (Fig. 1J), displaying increased intratumoral T cells similar to those reconstituted with WT BM cells under treatment with CD93 mAb (fig. S8F). We examined the effect of anti-CD93 on T cell migration in a nontumor model in which WT B6 mice were immunized with chicken ovalbumin (OVA) right after adoptively transferred with naive $CD8^+$ T cells from OVA-specific T cell receptor transgenic mice (OT-1). Treatment with anti-CD93 did not alter the distribution or proliferation of transferred OT-1 T cells at the immunization site, draining the lymph node or spleen (fig. S8, G and H).

We further demonstrated that retarded tumor growth by CD93 blockade requires the immune system. Treatment with anti-CD93 did not inhibit the growth of KPC tumors in immunodeficient non-obese diabetic (NOD)/severe combined immunodeficient NOD.Cg-*Prkdc^scid^Il2rg^tm1Wjl^*/SzJ (NSG) mice (fig. S9, A and B). However, there was improved vascular maturation in tumors treated with anti-CD93 mAb (fig. S9C), suggesting that vascular maturation itself by CD93 blockade does not affect tumor progression. We used depleting antibodies to further dissect the respective role of each immune cell type in anti-CD93–triggered antitumor immunity. The depletion of $CD8^+$ T cells by mAb throughout anti-CD93 treatment completely abrogated the effect of anti-CD93 on tumor growth inhibition; the removal of $CD4^+$ T cells slightly reduced the antitumor effect by anti-CD93 whereas NK cells had minimal effect (Fig. 5I). However, $CD8^+$ T cell depletion did not disrupt the effect of vascular maturation by anti-CD93 (fig. S9D), supporting that tumor vascular maturation by CD93 blockade is independent of antitumor immunity. Moreover, the depletion of $CD8^+$ T cells had no effect on the infiltration of $CD4^+$ T cells or NK cells in anti-CD93–treated tumors, suggesting that improved tumor vascular functions by anti-CD93 directly contribute to the increases of these immune cells within tumors (fig. S9E). Together, our results support that blockade of the CD93 pathway improves tumor vascular functions to promote T cell infiltration and antitumor immunity.

CD93 blockade facilitates cancer immunotherapy

PD-L1 expression can be up-regulated in tumor tissues in response to IFN-γ as a result of T cell activation (58). We reasoned that PD-L1 induction may be responsible for a limited antitumor effect of anti-CD93 therapy. We observed an up-regulation of PD-L1 expression on tumor tissues upon anti-CD93 treatment (Fig. 6A). Besides $CD31^+$ tumor ECs, we observed increases of PD-L1 expression in both tumor cells and $CD45^+$ leukocytes in anti-CD93–treated tumors compared with controls (Fig. 6B).

Increased intratumoral T cells and PD-L1 up-regulation by anti-CD93 prompted us to investigate whether blockade of the CD93/IGFBP7 interaction could facilitate cancer immunotherapy on the basis of immune normalization of the TME (59). Whereas the treatment with anti-CD93 or anti-PD1 mAb alone partially retarded KPC tumor growth, a combination of CD93 and PD1 mAbs profoundly inhibited tumor growth in mice (Fig. 6C). As a result, tumor weights in the combination group were reduced to only about 20% of the control group, and 3 of 10 mice in the combination group experienced complete regression (Fig. 6D). Analysis of immune cells within the tumors by combinatory therapy indicated substantially increased numbers of $CD45^+$ immune cells, including both $CD3^+$ and $CD8^+$ T cells, whereas the number of gMDSCs was reduced (Fig. 6E). Similarly, in the B16 melanoma mouse model, the inclusion of anti-CD93 improved the antitumor effect mediated by immune checkpoint blockers (ICB; PD1 and CTLA4 mAbs), as revealed by tumor growth (Fig. 6F) and mouse survival curves (Fig. 6G). The enhanced antitumor immunity by the combination of CD93 blockade and ICB was further verified by increased T cell infiltration within the tumors (Fig. 6H). Together, our results support that blockade of the CD93 pathway can sensitize tumors to ICB therapy.

Enrichment of the IGFBP7/CD93 pathway in human cancers resistant to anti-PD therapy

We next examined gene expressions of *IGFBP7* and *CD93* in patients with cancer under anti-PD therapy. In a phase 2 trial of patients with metastatic urothelial cancer receiving atezolizumab (anti–PD-L1 mAb) treatment (60), baseline expression of *IGFBP7* and *CD93* was higher in tumor tissues from nonresponders compared to tissues from responders (fig. S10A). In addition, in a small cohort of patients with metastatic melanoma under anti-PD1 treatment (61), baseline *IGFBP7* expression tended to be lower in patients who were responsive to anti-PD1 therapy compared to patients who did not benefit (fig. S10B). In summary, the IGFBP7/CD93 pathway in the TME may contribute to cancer resistance of anti-PD therapy in humans.

DISCUSSION

In this study, we have identified and characterized a previously unknown IGFBP7/CD93 interaction and demonstrated that this pathway contributes to abnormal tumor vasculature. Our findings further support that CD93 blockade can be a feasible approach for vascular normalization to facilitate cancer therapies. However, our study has several limitations. We conduct our experiments in two implanted mouse tumor models only; therefore, a spontaneous mouse tumor model to better mimic the human TME could be valuable. In addition, our analyses of tumor vasculature are done histologically at limited time points, which is subjective and incomplete. Advanced technology in imaging of live animals is needed to better record tumor vascular dynamics in response to CD93 blockade. Last, our clinical investigation of the impact of the CD93 pathway on ICB therapy in cancer remains limited.

Our studies provide a better understanding of the biological functions of IGFBP7. IGFBP7 was shown to be released from cancer cells and to act as a tumor suppressor that triggers tumor apoptosis and suppresses angiogenesis (62); IGF1R was proposed as the receptor and IGFBP7 binding disrupted the interaction between IGF1 and IGF1R to inhibit the expansion and aggressiveness of cancer stem-like cells (63, 64). On the other hand, IGFBP7 was shown to be up-regulated in tumor blood vessels and was capable of promoting vascular angiogenesis (50, 65). In addition to IGF1R, IGFBP7 has been shown to bind $\alpha v\beta 3$ (50), type IV collagen (66), and heparin sulfate (67). The functional outcome of these interactions is not well understood, but given the adhesion nature of these molecules because of carbohydrate involvement (68, 69), a proposed role of these interactions may be to retain IGFBP7 protein in the ECM. Our studies support that CD93 is the main receptor for the function of IGFBP7 on ECs. First, CD93 mediates both the binding and angiogenetic functions of IGFBP7 on ECs. Second, the interaction between CD93 and IGFBP7 is conserved between species and is specific with high affinity. Third, CD93 is the only cell surface binding partner that we found for IGFBP7 in our search from an array of more than 5000 surface proteins. Fourth, IGFBP7 mAb has functions similar to that of CD93 mAb in tumor vascular maturation and in facilitating immune cell infiltration. Last, IGFBP7 blocking mAb did not further increase the antitumor effect by anti-CD93, supporting that these two antibodies act on an overlapped pathway.

In addition to IGFBP7, MMRN2 was found recently to be a ligand for CD93 (45, 46). MMRN2 is also an ECM glycoprotein primarily expressed by ECs, and its expression is up-regulated by VEGF signaling (26, 27). MMRN2 and IGFBP7 do not compete each other for CD93 binding and our ELISA result indicated that they can form a heterotrimeric complex in vitro. Our CD93 mAb used for mouse tumor models happens to block CD93 binding to both ligands. It remains to be determined whether MMRN2 and IGFBP7 rely on each other or work independently to modulate EC functions via CD93. Further research into the respective roles for these two similar but nonredundant CD93 ligands in CD93-mediated EC functions is warranted.

Although CD93 blockade by mAb and genetic ablation both lead to tumor growth inhibition, detailed mechanisms can be different. In CD93$^{-/-}$ mice, tumor vasculature appears to be more permeable and less perfused and the antitumor mechanism may at least, in part, be related to vascular dysfunction (29, 31). In contrast, the treatment of CD93 mAb leads to better tumor vascular maturation and functions. This difference may be due to the fact that CD93 is completely lost in CD93$^{-/-}$ mice, whereas the ablation of CD93 signaling by a blocking antibody is transient and relatively incomplete. The antibody blockade may therefore lead to a normalization of CD93 signaling, because the expression of the CD93 pathway is considerably higher in tumor vessels than in the normal vasculature. This is very important to tumor vascular modulation: For example, different dosages of anti-VEGFR had different vascular effects on tumor vasculature (high dose of VEGFR mAb is antiangiogenic, whereas low dose of anti-VEGFR leads to vascular normalization) (11). Last, CD93 might have ligand-independent functions our CD93 blocking mAb does not disrupt; for instance, soluble CD93 (EGF-like domain) itself has potent angiogenic activities (70).

Our results imply that the IGFBP7/CD93 axis could be a safer therapeutic target for tumor vascular normalization, compared to VEGF inhibition. The CD93 pathway is highly enriched in the TME, as both IGFBP7 and CD93 are selectively up-regulated on tumor blood vessels in mouse and human tumors. Blockade of the CD93 pathway mainly led to improved vascular function, rather than an anti-angiogenic effect in the TME. CD93 mAb blockade had no clear effect on the vasculature in healthy organs, whereas an anti-VEGFR mAb markedly interfered with normal blood vessel homeostasis. Consistently, blockade of CD93 had no visible effect on vascular angiogenesis during wound healing, which is in sharp contrast to anti-VEGFR. The mild phenotypes observed in CD93$^{-/-}$, IGFBP7$^{-/-}$, and MMRN2$^{-/-}$ mice would further suggest that targeting this pathway can be safer than targeting the VEGF/VEGFR pathway (71–73). Together, our findings support that targeting the CD93 pathway may be a safe and durable approach to improve tumor vascular functions.

MATERIALS AND METHODS

Study design

This study was designed to investigate the role of the CD93/IGFBP7 interaction in tumor vasculature. Antitumor activity, vascular functions, and immune responses were evaluated in several mouse tumor models. This study was performed in accordance with protocols approved by the Institutional Animal Care and Use Committee at the University of Colorado Anschutz Medical Campus or the Uppsala County regional ethics committee (Dnr. 5.8.18-19429-2019). Animals with palpable tumors were randomly assigned to experimental groups such that mean tumor volumes were similar in each group to avoid biased results; however, experimenters were not blinded. Five to 10 animals per group were typically used for antitumor efficacy studies and analyses of tumor vasculature or immune cells. Figure legends contain information for sample sizes, experimental replicates, and statistical tests used.

Human tissues

Human pancreatic cancer and adjacent normal pancreas tissues were obtained from patients who underwent surgery at the University of Colorado Hospital according to an Institutional Review Board–approved protocol and patient consent. Other human cancer specimens were obtained from the Tissue Biobanking and Histology Shared Resource at the University of Colorado Cancer Center (UCCC).

Fusion proteins and antibodies

Expression constructs for IGFBP7 and CD93 fusion proteins were generated by cloning IGFBP7 and the extracellular domains of CD93 into a pmIgV expression vector, which contains the constant region of mouse IgG2a. Fusion proteins were expressed by transiently transfecting 293-F cells via 293fectin (Thermo Fisher Scientific), and fusion proteins were purified using a Protein A Sepharose column according to the manufacturer’s instruction (GE Healthcare). A hybridoma for rat anti-mouse CD93 mAb (clone 7C10) was generated by fusing SP2 myeloma with B cells from a rat immunized with mouse CD93-Ig. Hamster anti-mouse IGFBP7 mAbs (clones 2C6 and 6F1) were generated from hybridomas derived from the fusion of SP2 myeloma with B cells from Armenian hamster immunized with mouse IGFBP7-Ig. Hybridomas were adapted and cultured in serum-free hybridoma media (Life Technologies). Antibodies in supernatant were purified by HiTrap protein G affinity column (GE Healthcare). Purified mAbs for in vivo usage—including anti–mVEGFR-2 (DC101), anti-mPD1 (RMP1-14), anti-mCTLA4 (9D9), anti-mCD4 (GK1.5), anti-NK (NK1.1), and anti-mCD8β (53–5.8)—were purchased from Bio X Cell. Human IGFBP7 mAb (R003) and human CD93 mAb (MM01), obtained from Sino Biological, were used to block human IGFBP7-CD93 interaction. Anti–HIF-1α antibody (D1S7W, Cell Signaling Technology) and Human IGFBP7 mAb (R003) was used in Western blotting. Commercial antibodies, if not listed, were purchased from BioLegend.

Plasmids, chimeras, mutants, and transfection

The human cDNA library contained expression constructs coding about 5600 transmembrane proteins and 1000 secreted proteins, which were either purchased from companies Genecopoeia and Open Biosystems or were individually cloned into the pcDNA3.1 (−) vector in the laboratory. The detailed gene list and screening method for the GSRA were described previously (32). Human CD93-Fc was used to screen potential ligands in the whole GSRA library. The human cDNA library with 5600 transmembrane proteins was subsequently used to screen for possible surface receptors for IGFBP7. The IGFBP7-IGFBPL1 chimeras were generated by two-step PCR and were constructed into a fusion expression vector with Fc-tag. The chimeric proteins share the similar structure and contain the domains from IGFBP7 and IGFBPL1 that were interchanged at different cut sites. The supernatants were collected from individually transfected HEK293T cells for downstream binding assay. Fusion protein constructs for CD93 mutants or truncates were made by PCR and fused into pmIgV expression vectors containing the constant region of mouse IgG2a. All constructs were confirmed by sequencing. Lipofectamine 3000 kit (Invitrogen, L3000015) was used to perform transient transfection on HEK293T cells according to the protocol of the manufacturer. Eighteen to 24 hours after transfection, transfectants were collected for downstream analysis.

Flow cytometry

Staining and analysis of cell surface and intracellular molecules by flow cytometry followed the protocol previously described (74). Intracellular staining of cytokines IFN-γ and TNF-α was conducted after 4-hour stimulation of phorbol 12-myristate 13-acetate (25 ng/ml; Sigma-Aldrich) and ionomycin (1 μg/ml; Sigma-Aldrich), with the presence of 2 μM monensin (BioLegend). Staining antibodies were purchased from BioLegend, if not specified. Dead cells were excluded with Ghost Dye Red 780 (13-0865-T100, Tonbo Biosciences). Flow cytometric analysis was conducted with BD FACSCalibur, Beckman Coulter CytoFlex S, or BD LSRFortessa cell analyzer (BD Biosciences), and data were analyzed by FlowJo software (Tree Star Inc.) The binding kinetics (K_d) of anti-CD93 7C10 antibody binding to CD93 were measured by flow cytometry staining of Chinese hamster ovary (CHO) cells stably expressing mouse CD93.

MST experiment

IGFBP7 protein (R&D Systems, Minneapolis, MN) was labeled with a fluorescent dye using a Monolith His-Tag Labeling kit, RED-tris-NTA 2nd Generation (NanoTemper GMBH). From the 100 nM stock, sample was diluted into phosphate-buffered saline (PBS) + 0.05% P20 to a concentration of 20 nM, loaded into Premium MST Capillaries, and pretested for successful labeling and protein stability on a Monolith NT.115 Pico Instrument (NanoTemper GMBH). A stock solution of 5.9 μM recombinant human CD93 protein (R&D Systems) was diluted twofold 16 times in PBS + 0.05% P20 to create a dilution series spanning from 5.9 μM to 180 pM in range. IGFBP7 (20 nM) was added to each concentration 1:1 such that each sample contains a final concentration of 10 nM IGFBP7. Samples were loaded into MST Premium Capillaries and measured for MST on the aforementioned instrument. Experiments were conducted with the PICO Red detector, a laser power of 20% and Medium MST power. This experiment was repeated once with the same procedure for a total of two replicates. Data were analyzed using the MO Affinity Analysis software (NanoTemper GMBH).

Gene expression analyses

Genes that were significantly down-regulated in tumors under the treatment of VEGF inhibitors were selected from four different datasets: (i) RNA-seq of tumor tissues from Colo205 colon cancer xenograft (28), (ii) microarray of tumor tissues from a transgenic murine model (RIP-Tag2) of PNETs (27), (iii) microarray of tissues from human breast carcinoma xenograft model (MDA-MB-231) (27), and (iv) microarray of tumor tissues from U87-EV human glioblastoma xenograft (GSE37956) (26). The cutoff for selected genes from each dataset is $\log_2$ fold change < -0.5. We selected genes that were down-regulated in at least three of the four datasets for further analysis (table S1).

To systemically examine *IGFBP7* expression in tumor-associated ECs, we screened all the tumor-related studies for *IGFBP7* transcription by searching keyword “tumor” in EndoDB (75), an online database of EC transcriptomics data (https://endotheliomics.shinyapps.io/endodb/). Studies eligible for this meta-analysis include datasets containing both normal EC and tumor EC groups and normalized IGFBP7 transcriptomic data that are pooled from different studies in which the EC origin, isolation protocol, and array methods are the same. Meta-analysis was conducted by STATA software (version 14.0 with meta-analysis pr0012 plugin) by using random effects analysis model and standard mean difference for effect measurement. Published scRNA-seq data of human cancers about the cellular sources of CD93 in tumors were derived from Tumor Immune Single-cell Hub (TISCH) at http://tisch.comp-genomics.org.

Mouse tumor model

C57BL/6 mice at 6 to 8 weeks of age were purchased from the Jackson laboratory. The CD93$^{-/-}$ mouse was obtained from the Knockout Mouse Project (KOMP) Repository (www.komp.org) or generated as described (72). Two mouse tumor cell lines were used for implanted mouse tumor models: The KPC cell line, which is derived from *LSL-Kras*$^{G12D/+}$; *LSL-Trp53*$^{R172H/+}$; *Pdx-1-Cre* (KPC) transgenic mice, was obtained from L. Zheng’s laboratory at the Johns Hopkins University (34); B16 melanoma was originally obtained from the American Type Culture Collection.

For the orthotopic KPC tumor model, 1×10^5 KPC cells suspended in 50 µl of Hanks’ balanced salt solution were inoculated into the tail of the pancreas under appropriate anesthesia. Tumor tissues were harvested and analyzed 21 days after inoculation. For the subcutaneous KPC model, KPC cells (4×10^5) were subcutaneously injected into the right flank of C57BL/6 mice or NOD.Cg-*Prkdc*^{scid}*Il2rg*^{tm1Wjl}/SzJ (NSG) mice (the Jackson laboratory). After tumors became palpable, mice were randomized into different treatment groups on the basis of tumor volume, which was calculated as $1/2 \times (\text{length} \times \text{width}^2)$. To induce maximal blocking capacity without specific kinetics, we selected a saturated procedure for therapeutic antibodies: 400 µg per mouse (~20 mg/kg) was intraperitoneally injected twice a week for up to a total of four treatments. Control mice were treated with the same amount of rat or hamster Ig. Tumor measurements were taken every 2 or 3 days with a caliper. Mice were euthanized, and tumor tissues were excised for detailed analysis 8 to 15 days after the first treatment. Experiments for FITC-lectin perfusion and Hypoxyprobe assay were performed at day 8 after the first treatment. For the combination therapy of PD1 (clone RMP1-14, Bio X Cell) and CD93 antibodies, mice with established KPC tumors were started with the treatment of antibodies at twice a week for 2 weeks. To deplete NK, $CD4^+$, or $CD8^+$ T cells, anti-NK1.1 (PK136), anti-mCD4 (GK1.5), or anti-mouse CD8β (clone 53–5.8) at 300 μg per mouse was interperitoneally administered 1 day before the first CD93 mAb treatment and repeated at day 7 at a 200-μg dosage.

For the B16 tumor model, C57BL/6 mice were subcutaneously inoculated with B16 melanoma at 1×10^5 (Figs. 1 and 6) or 2×10^5 (Fig. 4) per mouse. Once tumors became palpable, therapeutic antibodies at 400 μg per mouse were intraperitoneally injected twice a week for a total of four treatments. CD93 chimeric mice were generated by transferring 2×10^6 BM cells from $CD93^{-/-}$ or WT mice into lethally irradiated WT B6 mice [1100 rads (2 × 550 rads) using a gamma irradiator with cesium-137]. Chimeric mice were used for tumor experiments 12 weeks after reconstitution. For the combination of anti-CD93 and ICB therapy, mice with palpable tumors were treated with control (rat Ig), CD93 mAb, ICB (anti-CTLA4 + anti-PD1 at 150 μg each), or CD93 mAb and ICB twice a week. Tumor tissues were obtained for analysis 14 days after the first treatment. For the survival study, mice with tumor volume exceeding 1200 mm^3 were euthanized for the calculation of survival curve.

Immunohistochemistry and IF staining

The immunohistochemistry staining protocol has been described previously (76). Mouse tissue samples were collected and frozen on dry ice using optimum cutting temperature mounting fluid. The frozen blocks were sectioned at 7 μm and mounted on glass slides. The slides were fixed in acetone, blocked with 2.5% goat serum, incubated with primary antibodies overnight at 4°C, washed and incubated with secondary antibodies for 1 hour at room temperature, and counterstained with 4′,6-diamidino-2-phenylindole for 10 min. The slides were then cleared and mounted. If not specified, then images were taken by Nikon Eclipse TE2000-E upright microscope or Olympus FV1000 FCS confocal laser scanning microscope (University of Colorado Anschutz Medical Campus, Advanced Light Microscopy Core Facility) and analyzed using SlideBook software (Version 6, Intelligent Imaging Inc.) and ImageJ [Version 1.52 K, National Institutes of Health (NIH)]. Primary antibodies used for immunostaining include anti-human IGFBP7 (R115, Sino Biological), anti-human CD31 (JC/70A, Thermo Fisher Scientific), anti-human CD93 (HPA009300, Sigma-Aldrich), anti-mouse CD31 (390), anti-mouse CD3e (145-2C11), anti-mouse CD45.2 (104), anti-mouse CD4 (RM4-5), anti-mouse CD8a (53-6.7), anti-mouse ALDH1A3 (Abcam, ab129815), anti-mouse BNIP3 (Invitrogen, PA5-11402), anti-mouse MAFA (Bethyl Laboratories, A300-611A), anti-mouse Ki-67 (16A8), anti-CC3 (D175, Cell Signaling Technology), anti-mouse B7-H1 (10F.9G2), anti-mouse IGFBP7 (6F1), anti-mouse CD93 (7C10) and anti-mouse CD54 (ICAM1, YN1/1.7.4), anti-mouse HEV marker (MECA79, 53-6036-82, Invitrogen), anti-mouse ANG2 (ab8452, Abcam), and anti-mouse HIF-1a (D1S7W, Cell Signaling Technology). NG2 (Cy3-conjugated polyclonal antibody, AB5320C3, Millipore), αSMA (1A4, eFluor 660 conjugated, Invitrogen), and PDGFRβ (14-1402-82, Invitrogen) staining were used for the evaluation of vascular surrounding pericytes. Activated integrin β1 was stained with CD29 mAb (clone 9EG7) from BD Pharmingen.

Hypoxia, perfusion, and vascular leakage measurement

Tumor hypoxia was detected by injecting pimonidazole hydrochloride (30 mg/kg; Hypoxyprobe kit) into tumor-bearing mice 1 hour before tumors were harvested. To detect the formation of pimonidazole adducts, tumor frozen sections were stained with Allophycocyanin (APC)-Hypoxyprobe mAb following the manufacturer’s instruction. To assess drug delivery in tumors, doxorubicin (Sigma-Aldrich) at 30 mg/kg was intravenously injected into tumor-bearing mice 1 hour before tumors were harvested for analysis. Doxorubicin in frozen tissue sections was detected by fluorescence microscope with setting of excitation and emission wavelength at 488 and 570 nm. Tumor perfusion was quantified on tumor cryosections after intravenous injection of 50-μg FITC-labeled *Lycopersicon esculentum* (Tomato) lectin (FL-1171, Vector Laboratories) into tumor-bearing mice 10 min before tumors were harvested for analysis. The perfused tumor vasculature was defined as FITC^+ $\mathrm{CD31}^+$ vessels. Tumor vascular leakage was evaluated by intravenous injection of 5 mg of FITC-labeled dextran (40 kDa; FD40S Sigma-Aldrich) into tumor-bearing mice 30 min before tumors were harvested for analysis. Thick cryosections (30 μm) were made for downstream IF staining (CD31) and quantification (FITC^+ leaked area/tumor area).

RNA-seq and data analysis

Total RNA was extracted and purified using QIAGEN RNeasy Mini Kit (catalog no. 74104) from tumor ECs, which were isolated by fluorescence-activated cell sorting ($\mathrm{CD31}^+\mathrm{CD45}^-$ population) from established subcutaneous KPC tumors after 48 hours of antibody treatment. The mRNA libraries were constructed using the Takara SMARTer Stranded Total RNA-seq Kit v2-Pico Input Mammalian (catalog no. 634411). A total of 150–base pair paired-end RNA-seq was performed on Illumina NovaSEQ 6000 platform, and the RNA-seq data were generated by the Genomics and Microarray Shared Resource at UCCC. The data were processed using STAR software (Galaxy Ver. 2.7.5b) for mapping and DESeq2 (Ver.1.28.1) for differential analysis. The volcano plot and GO biological pathways analysis were generated using GraphPad Prism 7.0 software and RStudio 1.3.1073 (with GO.db 3.11.4).

For patients with metastatic urothelial cancer undergoing treatment with an anti–PD-L1 agent (atezolizumab), raw gene expression and patient phenotype data were obtained via theIMvigor210CoreBiologies package (60). Patients with complete or partial response were classified as “Responders” and those with stable or progressive disease were classified as “Nonresponders.” Genes with mean raw expression counts less than 1 were removed, and remaining raw counts were normalized to counts per million using the edgeR R package (77). Gene expression of *CD93* and *IGFBP7* was plotted according to response to PD-L1 blockade. Groups were compared using a Wilcoxon rank sum test. Gene expression data for patients with melanoma undergoing anti-PD1 therapy were obtained from Gene Expression Omnibus (GEO): GSE78220 (61). Gene expression of *CD93* and *IGFBP7* in melanoma was plotted according to response to PD1 blockade. TCGA and GTEx datasets were analyzed through the Gene Expression Profiling Interactive Analysis, a web-based tool for cancer and normal gene expression analyses (78).

In a xenograft colon cancer mouse model under the treatment of aflibercept (51), we examined *IGFBP7* expression in tumor ECs in response to VEGF inhibition. Gene expression matrices of scRNA-seq data from control_24h (GSM2994872) and drug_24h (GSM2994873) were downloaded from the GEO database (GSE110501). Two matrices were filtered to keep genes expressed in at least three cells using Seurat 3.0 software tool. Data were then normalized, scaled, and integrated using 1000 most variable genes for embedding (canonical correlation analysis). Integrated data were then subject to principal components analysis and clustering using Louvain algorithm. Cell clustering result was presented in a two-dimensional Uniform Manifold Approximation and Projection (UMAP). Endothelial marker gene *pecam1* was used to identify this population in UMAP. Gene expression in ECs between control and drug-treated conditions was presented in a violin plot.

Quantitative PCR

qPCR (PowerUp SYBR Green Master Mix, Applied Biosystems, no. A25741 on QuantStudio 3 instrument) was performed to validate changes of gene expression identified by RNA-seq. KPC tumor ECs were isolated to generate cDNA for qPCR with the same protocol for RNA-seq but in an independent experiment. The knockdown of gene expression in HUVEC cells was confirmed by qPCR. The primers used for qPCR are mouse *glyceraldehyde-3-phosphate dehydrogenase* (*GAPDH*) (forward, 5′-tcccactcttccaccttcga-3′; reverse, 5′-tagggcctctcttgctcagt-3′), mouse *ALDH1A3* (forward, 5′-tcggggacagtctggatcaa-3′; reverse, 5′-tcaggggttcttctcctcga-3′), mouse *BNIP3* (forward, 5′-tctcatctgctggccattgg-3′; reverse, 5′-tgcaaacacccaaggaccat-3′), mouse *GATA1* (forward, 5′-accactacaacactctggcg-3′; reverse, 5′-attcgacccccgcttctttt-3′), mouse *HMGCS2* (forward, 5′-tgagatgcatcgcaggaagt-3′; reverse, 5′-ccgttcaccacagagcagat-3′), mouse *MAFA* (forward, 5′-aaggagcgggacctgtacaa-3′; reverse, 5′-gtccggcactcacagaaaga-3′), mouse *SFRP2* (forward, 5′-aggtgtgtgaagcctgcaaa-3′; reverse, 5′-ttgagccacagcacggattt-3′), human *GAPDH* (forward, 5′-ggagcgagatccctccaaaat-3′; reverse, 5′-ggctgttgtcatacttctcatgg-3′), human *ALDH1A3* (forward, 5′-agagtctggaacggtctgga-3′; reverse, 5′-atgtttgaggaaggagcccc-3′), human *BNIP3* (forward, 5′-tccttccatctctgctgctc-3′; reverse, 5′-aaacacaagtgacgtggcca-3′), and human *MAFA* (forward, 5′-atgcttcgtcgctctttgga-3′; reverse, 5′-aaactttcaacgagtcggcg-3′).

Statistical analysis

Prism software (GraphPad) was used for all statistical analyses. Unpaired two-tailed Student's *t* test was used to compare two groups. One-way analysis of variance (ANOVA) was used for a comparison of more than two groups. Tumor-growth curves were analyzed by two-way ANOVA test. Kaplan-Meier survival curves were used to estimate survival rates for different treatment groups. Survival curves were compared with the log-rank (Mantel-Cox) test. Data were presented as means ± SEM, if not otherwise specified. *P* values lower than 0.05 were considered statistically significant.

Supplementary Material

Refer to Web version on PubMed Central for supplementary material.

Acknowledgments:

We thank B. Cadugan for manuscript editing, the Human Immunology & Immunotherapy Initiative (HI3) and the Advanced Light Microscopy Core Facility at the University of Colorado Anschutz Medical Campus (AMC) for flow cytometry and immunofluorescence analyses, the Tissue Biobanking and Histology Shared Resource at UCCC for obtaining cancer specimens, the Functional Genomics Shared Resource at UCCC for shRNA constructs, the Genomics and Microarray Shared Resource at UCCC for RNA-seq, the Biophysics Core at the University of Colorado AMC for microscale thermophoresis (MST) analysis, L. Zheng at Johns Hopkins University for the KPC cell line, and R. Kedl for animal irradiation.

Funding:

This study is partially supported by NIH P30CA046934 (to R.D.S.); the Wings of Hope for Pancreatic Research (to Y.Z.); the Research Scholar Grant, RSG-17-106-01 LIB, from the American Cancer Society (to Y.Z.); NIH R01HL143803 (to S.A.); NIH R01-DE028420 (to X.J.W.); VA Merit Award I01 BX003232 (to X.J.W.); NIH CA196530 (to L.C.); and an endowment from United Technologies Corporation (to L.C.).

Competing interests:

Y.Z. and R.D.S. receive sponsored research grant support from GlaxoSmithKline. Y.Z. consults for Dynamicure Biotechnology. R.D.S consults for NOILE Immune. L.C. serves on the scientific advisory board/board of directors of NextCure, Zai Lab, Pfizer, Vcanbio, Junshi, GenomiCare, and Tayu and has sponsored research funds from NextCure, Tayu, and Boehringer Ingelheim. S.Y. is employed by TopAlliance Biosciences Inc. and Shanghai Junshi Biosciences Inc. L.C., R.D.S, Y.S., and Y.Z. filed a patent (PCT/US2020/052681) titled, “Methods and compositions for treating a disease or disorder,” containing some of the findings in the manuscript.

Data and materials availability:

All data associated with this study are present in the paper or the Supplementary Materials. mAbs for mCD93 (7C10) and mIGFBP7 (2C6) are available from University of Colorado Anschutz Medical Campus upon completion of a material transfer agreement. The RNA-seq data of tumor-associated ECs in Fig. 1F have been deposited in the GEO under accession no. GSE173658.

REFERENCES AND NOTES

1. De Palma M, Biziato D, Petrova TV, Microenvironmental regulation of tumour angiogenesis. Nat. Rev. Cancer 17, 457–474 (2017). [PubMed: 28706266]
2. Carmeliet P, Jain RK, Angiogenesis in cancer and other diseases. Nature 407, 249–257 (2000). [PubMed: 11001068]
3. McDonald DM, Baluk P, Significance of blood vessel leakiness in cancer. Cancer Res 62, 5381–5385 (2002). [PubMed: 12235011]
4. Dreher MR, Liu W, Michelich CR, Dewhirst MW, Yuan F, Chilkoti A, Tumor vascular permeability, accumulation, and penetration of macromolecular drug carriers. J. Natl. Cancer Inst 98, 335–344 (2006). [PubMed: 16507830]
5. Lanitis E, Irving M, Coukos G, Targeting the tumor vasculature to enhance T cell activity. Curr. Opin. Immunol 33, 55–63 (2015). [PubMed: 25665467]
6. Hatfield SM, Kjaergaard J, Lukashev D, Schreiber TH, Belikoff B, Abbott R, Sethumadhavan S, Philbrook P, Ko K, Cannici R, Thayer M, Rodig S, Kutok JL, Jackson EK, Karger B, Podack ER, Ohta A, Sitkovsky MV, Immunological mechanisms of the antitumor effects of supplemental oxygenation. Sci. Transl. Med 7, 277ra230 (2015).

7. Chanmee T, Ontong P, Konno K, Itano N, Tumor-associated macrophages as major players in the tumor microenvironment. Cancer 6, 1670–1690 (2014).
8. Huber V, Camisaschi C, Berzi A, Ferro S, Lugini L, Triulzi T, Tuccitto A, Tagliabue E, Castelli C, Rivoltini L, Cancer acidity: An ultimate frontier of tumor immune escape and a novel target of immunomodulation. Semin. Cancer Biol 43, 74–89 (2017). [PubMed: 28267587]
9. Ranieri G, Patruno R, Ruggieri E, Montemurro S, Valerio P, Ribatti D, Vascular endothelial growth factor (VEGF) as a target of bevacizumab in cancer: From the biology to the clinic. Curr. Med. Chem 13, 1845–1857 (2006). [PubMed: 16842197]
10. Carmeliet P, Jain RK, Molecular mechanisms and clinical applications of angiogenesis. Nature 473, 298–307 (2011). [PubMed: 21593862]
11. Huang Y, Yuan J, Righi E, Kamoun WS, Ancukiewicz M, Nezivar J, Santosuosso M, Martin JD, Martin MR, Vianello F, Leblanc P, Munn LL, Huang P, Duda DG, Fukumura D, Jain RK, Poznansky MC, Vascular normalizing doses of antiangiogenic treatment reprogram the immunosuppressive tumor microenvironment and enhance immunotherapy. Proc. Natl. Acad. Sci. U.S.A 109, 17561–17566 (2012). [PubMed: 23045683]
12. Huang Y, Stylianopoulos T, Duda DG, Fukumura D, Jain RK, Benefits of vascular normalization are dose and time dependent—Letter. Cancer Res 73, 7144–7146 (2013). [PubMed: 24265277]
13. Jain RK, Normalization of tumor vasculature: An emerging concept in antiangiogenic therapy. Science 307, 58–62 (2005). [PubMed: 15637262]
14. Hamzah J, Jugold M, Kiessling F, Rigby P, Manzur M, Marti HH, Rabie T, Kaden S, Gröne H-J, Hämmerling GJ, Arnold B, Ganss R, Vascular normalization in *Rgs5*-deficient tumours promotes immune destruction. Nature 453, 410–414 (2008). [PubMed: 18418378]
15. Huang Y, Goel S, Duda DG, Fukumura D, Jain RK, Vascular normalization as an emerging strategy to enhance cancer immunotherapy. Cancer Res 73, 2943–2948 (2013). [PubMed: 23440426]
16. Tian L, Goldstein A, Wang H, Lo HC, Kim IS, Welte T, Sheng K, Dobrolecki LE, Zhang X, Putluri N, Phung TL, Mani SA, Stossi F, Sreekumar A, Mancini MA, Decker WK, Zong C, Lewis MT, Zhang XH-F, Mutual regulation of tumour vessel normalization and immunostimulatory reprogramming. Nature 544, 250–254 (2017). [PubMed: 28371798]
17. Fukurnura D, Kloepper J, Amoozgar Z, Duda DG, Jain RK, Enhancing cancer immunotherapy using antiangiogenics: Opportunities and challenges. Nat. Rev. Clin. Oncol 15, 325–340 (2018). [PubMed: 29508855]
18. Makker V, Rasco D, Vogelzang NJ, Brose MS, Cohn AL, Mier J, Di Simone C, Hyman DM, Stepan DE, Dutcus CE, Schmidt EV, Guo M, Sachdev P, Shumaker R, Aghajanian C, Taylor M, Lenvatinib plus pembrolizumab in patients with advanced endometrial cancer: An interim analysis of a multicentre, open-label, single-arm, phase 2 trial. Lancet Oncol 20, 711–718 (2019). [PubMed: 30922731]
19. Aggen DH, Drake CG, Rini BI, Targeting PD-1 or PD-L1 in metastatic kidney cancer: Combination therapy in the first-line setting. Clin. Cancer Res 26, 2087–2095 (2020). [PubMed: 31948999]
20. Socinski MA, Jotte RM, Cappuzzo F, Orlandi F, Stroyakovskiy D, Nogami N, Rodríguez-Abreu D, Moro-Sibilot D, Thomas CA, Barlesi F, Finley G, Kelsch C, Lee A, Coleman S, Deng Y, Shen Y, Kowanetz M, Lopez-Chavez A, Sandler A, Reck M; IMpower150 Study Group, Atezolizumab for first-line treatment of metastatic nonsquamous NSCLC. N. Engl. J. Med 378, 2288–2301 (2018). [PubMed: 29863955]
21. Liu JF, Herold C, Gray KP, Penson RT, Horowitz N, Konstantinopoulos PA, Castro CM, Hill SJ, Curtis J, Luo W, Matulonis UA, Cannistra SA, Dizon DS, Assessment of combined nivolumab and bevacizumab in relapsed ovarian cancer: A phase 2 clinical trial. JAMA Oncol 5, 1731–1738 (2019). [PubMed: 31600397]
22. Finn RS, Qin S, Ikeda M, Galle PR, Ducreux M, Kim T-Y, Kudo M, Breder V, Merle P, Kaseb AO, Li D, Verret W, Xu D-Z, Hernandez S, Liu J, Huang C, Mulla S, Wang Y, Lim HY, Zhu AX, Cheng A-L; IMbrave150 Investigators, Atezolizumab plus bevacizumab in unresectable hepatocellular carcinoma. N. Engl. J. Med 382, 1894–1905 (2020). [PubMed: 32402160]

23. Ferrara N, The role of VEGF in the regulation of physiological and pathological angiogenesis. EXS, 209–231 (2005). [PubMed: 15617481]
24. Hurwitz H, Fehrenbacher L, Novotny W, Cartwright T, Hainsworth J, Heim W, Berlin J, Baron A, Griffing S, Holmgren E, Ferrara N, Fyfe G, Rogers B, Ross R, Kabbinavar F, Bevacizumab plus irinotecan, fluorouracil, and leucovorin for metastatic colorectal cancer. N. Engl. J. Med 350, 2335–2342 (2004). [PubMed: 15175435]
25. Seaman S, Stevens J, Yang MY, Logsdon D, Graff-Cherry C, Croix BS, Genes that distinguish physiological and pathological angiogenesis. Cancer Cell 11, 539–554 (2007). [PubMed: 17560335]
26. Masiero M, Simões FC, Han HD, Snell C, Peterkin T, Bridges E, Mangala LS, Wu SY-Y, Pradeep S, Li D, Han C, Dalton H, Lopez-Berestein G, Tuynman JB, Mortensen N, Li J-L, Patient R, Sood AK, Banham AH, Harris AL, Buffa FM, A core human primary tumor angiogenesis signature identifies the endothelial orphan receptor ELTD1 as a key regulator of angiogenesis. Cancer Cell 24, 229–241 (2013). [PubMed: 23871637]
27. Brauer MJ, Zhuang G, Schmidt M, Yao J, Wu X, Kaminker JS, Jurinka SS, Kolumam G, Chung AS, Jubb A, Modrusan Z, Ozawa T, James CD, Phillips H, Haley B, Tam RNW, Clermont AC, Cheng JH, Yang SX, Swain SM, Chen D, Scherer SJ, Koeppen H, Yeh R-F, Yue P, Stephan J-P, Hegde P, Ferrara N, Singh M, Bais C, Identification and analysis of *in vivo* VEGF downstream markers link VEGF pathway activity with efficacy of anti-VEGF therapies. Clin. Cancer Res 19, 3681–3692 (2013). [PubMed: 23685835]
28. Baker LCJ, Boult JKR, Thomas M, Koehler A, Nayak T, Tessier J, Ooi C-H, Birzele F, Belousov A, Zajac M, Horn C, LeFave C, Robinson SP, Acute tumour response to a bispecific Ang-2-VEGF-A antibody: Insights from multiparametric MRI and gene expression profiling. Brit. J. Cancer 115, 691–702 (2016). [PubMed: 27529514]
29. Langenkamp E, Zhang L, Lugano R, Huang H, Elhassan TEA, Georganaki M, Bazzar W, Lööf J, Trendelenburg G, Essand M, Pontén F, Smits A, Dimberg A, Elevated expression of the C-type lectin CD93 in the glioblastoma vasculature regulates cytoskeletal rearrangements that enhance vessel function and reduce host survival. Cancer Res 75, 4504–4516 (2015). [PubMed: 26363010]
30. Galvagni F, Nardi F, Maida M, Bernardini G, Vannuccini S, Petraglia F, Santucci A, Orlandini M, CD93 and dystroglycan cooperation in human endothelial cell adhesion and migration. Oncotarget 7, 10090–10103 (2016). [PubMed: 26848865]
31. Lugano R, Vemuri K, Yu D, Bergqvist M, Smits A, Essand M, Johansson S, Dejana E, Dimberg A, CD93 promotes β1 integrin activation and fibronectin fibrillogenesis during tumor angiogenesis. J. Clin. Invest 128, 3280–3297 (2018). [PubMed: 29763414]
32. Wang J, Sanmamed MF, Datar I, Su TT, Ji L, Sun J, Chen L, Chen Y, Zhu G, Yin W, Zheng L, Zhou T, Badri T, Yao S, Zhu S, Boto A, Sznol M, Melero I, Vignali DAA, Schalper K, Chen L, Fibrinogen-like protein 1 is a major immune inhibitory ligand of LAG-3. Cell 176, 334–347.e12 (2019). [PubMed: 30580966]
33. Olsen RS, Lindh M, Vorkapic E, Andersson RE, Zar N, Löfgren S, Dimberg J, Matussek A, Wågsäter D, CD93 gene polymorphism is associated with disseminated colorectal cancer. Int. J. Colorectal Dis 30, 883–890 (2015). [PubMed: 26008729]
34. Foley K, Rucki AA, Xiao Q, Zhou D, Leubner A, Mo G, Kleponis J, Wu AA, Sharma R, Jiang Q, Anders RA, Iacobuzio-Donahue CA, Hajjar KA, Maitra A, Jaffee EM, Zheng L, Semaphorin 3D autocrine signaling mediates the metastatic role of annexin A2 in pancreatic cancer. Sci. Signal 8, ra77 (2015). [PubMed: 26243191]
35. Bergers G, Song S, The role of pericytes in blood-vessel formation and maintenance. Neuro Oncol 7, 452–464 (2005). [PubMed: 16212810]
36. Herbert SP, Stainier DYR, Molecular control of endothelial cell behaviour during blood vessel morphogenesis. Nat. Rev. Mol. Cell Biol 12, 551–564 (2011). [PubMed: 21860391]
37. Jurasz P, Yurkova N, Kirshenbaum L, Stewart DJ, VEGF masks BNIP$_3$-mediated apoptosis of hypoxic endothelial cells. Angiogenesis 14, 199–207 (2011). [PubMed: 21318419]
38. Káňová E, Tkáčová Z, Bhide K, Kulkarni A, Jiménez-Munguía I, Mertinková P, Drážovská M, Tyagi P, Bhide M, Transcriptome analysis of human brain microvascular endothelial cells response to *Neisseria meningitidis* and its antigen MafA using RNA-seq. Sci. Rep 9, 18763 (2019). [PubMed: 31822804]

39. Zou KJ, Hu Y, Li MS, Wang HL, Zhang YH, Huang L, Xie YW, Li SY, Dai XG, Xu WF, Ke ZY, Gong ST, Wang YD, Potential role of HMGCS2 in tumor angiogenesis in colorectal cancer and its potential use as a diagnostic marker. Can. J. Gastroenterol. Hepatol 2019, 8348967 (2019). [PubMed: 31355161]

40. Xie X, Urabe G, Marcho L, Stratton M, Guo L-W, Kent CK, ALDH1A3 regulations of matricellular proteins promote vascular smooth muscle cell proliferation. Iscience 19, 872–882 (2019). [PubMed: 31513972]

41. Courtwright A, Siamakpour-Reihani S, Arbiser JL, Banet N, Hilliard E, Fried L, Livasy C, Ketelsen D, Nepal DB, Perou CM, Patterson C, Klauber-DeMore N, Secreted frizzle-related protein 2 stimulates angiogenesis via a calcineurin/NFAT signaling pathway. Cancer Res 69, 4621–4628 (2009). [PubMed: 19458075]

42. Fan C, Ouyang P, Timur AA, He P, You S-A, Hu Y, Ke T, Driscoll DJ, Chen QY, Wang QK, Novel roles of GATA1 in regulation of angiogenic factor AGGF1 and endothelial cell function. J. Biol. Chem 284, 23331–23343 (2009). [PubMed: 19556247]

43. Greenlee-Wacker MC, Galvan MD, Bohlson SS, CD93: Recent advances and implications in disease. Curr. Drug Targets 13, 411–420 (2012). [PubMed: 22206251]

44. Yang YL, Zhang Y, Cao ZQ, Ji H, Yang XJ, Iwamoto H, Wahlberg E, Länne T, Sun BC, Cao YH, Anti-VEGF– and anti-VEGF receptor–induced vascular alteration in mouse healthy tissues. Proc. Natl. Acad. Sci. U.S.A 110, 12018–12023 (2013). [PubMed: 23818623]

45. Khan KA, Naylor AJ, Khan A, Noy PJ, Mambretti M, Lodhia P, Athwal J, Korzystka A, Buckley CD, Willcox BE, Mohammed F, Bicknell R, Multimerin-2 is a ligand for group 14 family C-type lectins CLEC14A, CD93 and CD248 spanning the endothelial pericyte interface. Oncogene 36, 6097–6108 (2017). [PubMed: 28671670]

46. Galvagni F, Nardi F, Spiga O, Trezza A, Tarticchio G, Pellicani R, Andreuzzi E, Caldi E, Toti P, Tosi GM, Santucci A, Iozzo RV, Mongiat M, Orlandini M, Dissecting the CD93-multimerin 2 interaction involved in cell adhesion and migration of the activated endothelium. Matrix Biol 64, 112–127 (2017). [PubMed: 28912033]

47. Zhu S, Xu F, Zhang J, Ruan W, Lai M, Insulin-like growth factor binding protein-related protein 1 and cancer. Clin. Chim. Acta 431, 23–32 (2014). [PubMed: 24513543]

48. Cai Z, Chen HT, Boyle B, Rupp F, Funk WD, Dedera DA, Identification of a novel insulin-like growth factor binding protein gene homologue with tumor suppressor like properties. Biochem. Biophys. Res. Commun 331, 261–266 (2005). [PubMed: 15845387]

49. Schödel J, Oikonomopoulos S, Ragoussis J, Pugh CW, Ratcliffe PJ, Mole DR, High-resolution genome-wide mapping of HIF-binding sites by ChIP-seq. Blood 117, e207–e217 (2011). [PubMed: 21447827]

50. Komiya E, Sato H, Watanabe N, Ise M, Higashi S, Miyagi Y, Miyazaki K, Angiomodulin, a marker of cancer vasculature, is upregulated by vascular endothelial growth factor and increases vascular permeability as a ligand of integrin $\alpha v\beta 3$. Cancer Med 3, 537–549 (2014). [PubMed: 24737780]

51. Zhao Q, Eichten A, Parveen A, Adler C, Huang Y, Wang W, Ding Y, Adler A, Nevins T, Ni M, Wei Y, Thurston G, Single-cell transcriptome analyses reveal endothelial cell heterogeneity in tumors and changes following antiangiogenic treatment. Cancer Res 78, 2370–2382 (2018). [PubMed: 29449267]

52. Hooper AT, Shmelkov SV, Gupta S, Milde T, Bambino K, Gillen K, Goetz M, Chavala S, Baljevic M, Murphy AJ, Valenzuela DM, Gale NW, Thurston G, Yancopoulos GD, Vahdat L, Evans T, Rafii S, Angiomodulin is a specific marker of vasculature and regulates vascular endothelial growth factor-A–dependent neoangiogenesis. Circ. Res 105, 201–208 (2009). [PubMed: 19542015]

53. Chae S-S, Kamoun WS, Farrar CT, Kirkpatrick ND, Niemeyer E, de Graaf AM, Sorensen AG, Munn LL, Jain RK, Fukumura D, Angiopoietin-2 interferes with anti-VEGFR2-induced vessel normalization and survival benefit in mice bearing gliomas. Clin. Cancer Res 16, 3618–3627 (2010). [PubMed: 20501615]

54. Park J-S, Kim I-K, Han S, Park I, Kim C, Bae J, Oh SJ, Lee S, Kim JH, Woo D-C, He Y, Augustin HG, Kim I, Lee D, Koh GY, Normalization of tumor vessels by Tie2 Activation and Ang2 inhibition enhances drug delivery and produces a favorable tumor microenvironment. Cancer Cell 30, 953–967 (2016). [PubMed: 27960088]

55. Hakanpaa L, Sipila T, Leppanen V-M, Gautam P, Nurmi H, Jacquemet G, Eklund L, Ivaska J, Alitalo K, Saharinen P, Endothelial destabilization by angiopoietin-2 via integrin β1 activation. Nat. Commun 6, 5962 (2015). [PubMed: 25635707]

56. Schmittnaegel M, Rigamonti N, Kadioglu E, Cassara A, Rmili CW, Kiialainen A, Kienast Y, Mueller H-J, Ooi C-H, Laoui D, De Palma M, Dual angiopoietin-2 and VEGFA inhibition elicits antitumor immunity that is enhanced by PD-1 checkpoint blockade. Sci. Transl. Med 9, eaak9670 (2017). [PubMed: 28404865]

57. Allen E, Jabouille A, Rivera LB, Lodewijckx I, Missiaen R, Steri V, Feyen K, Tawney J, Hanahan D, Michael IP, Bergers G, Combined antiangiogenic and anti-PD-L1 therapy stimulates tumor immunity through HEV formation. Sci. Transl. Med 9, eaak9679 (2017). [PubMed: 28404866]

58. Taube JM, Anders RA, Young GD, Xu HY, Sharma R, McMiller TL, Chen SM, Klein AP, Pardoll DM, Topalian SL, Chen LP, Colocalization of inflammatory response with B7-H1 expression in human melanocytic lesions supports an adaptive resistance mechanism of immune escape. Sci. Transl. Med 4, 127ra137 (2012).

59. Sanmamed MF, Chen LP, A paradigm shift in cancer immunotherapy: From enhancement to normalization. Cell 175, 313–326 (2018). [PubMed: 30290139]

60. Mariathasan S, Turley SJ, Nickles D, Castiglioni A, Yuen K, Wang Y, Kadel III EE, Koeppen H, Astarita JL, Cubas R, Jhunjhunwala S, Banchereau R, Yang Y, Guan Y, Chalouni C, Ziai J, Şenbabaoğlu Y, Santoro S, Sheinson D, Hung J, Giltnane JM, Pierce AA, Mesh K, Lianoglou S, Riegler J, Carano RAD, Eriksson P, Höglund M, Somarriba L, Halligan DL, van der Heijden MS, Loriot Y, Rosenberg JE, Fong L, Mellman I, Chen DS, Green M, Derleth C, Fine GD, Hegde PS, Bourgon R, Powles T, TGFβ attenuates tumour response to PD-L1 blockade by contributing to exclusion of T cells. Nature 554, 544–548 (2018). [PubMed: 29443960]

61. Hugo W, Zaretsky JM, Sun L, Song C, Moreno BH, Hu-Lieskovan S, Berent-Maoz B, Pang J, Chmielowski B, Cherry G, Seja E, Lomeli S, Kong X, Kelley MC, Sosman JA, Johnson DB, Ribas A, Lo RS, Genomic and transcriptomic features of response to anti-PD-1 therapy in metastatic melanoma. Cell 165, 35–44 (2016). [PubMed: 26997480]

62. Wajapeyee N, Serra RW, Zhu X, Mahalingam M, Green MR, Oncogenic BRAF induces senescence and apoptosis through pathways mediated by the secreted protein IGFBP7. Cell 132, 363–374 (2008). [PubMed: 18267069]

63. Cao Z, Scandura JM, Inghirami GG, Shido K, Ding B-S, Rafii S, Molecular checkpoint decisions made by subverted vascular niche transform indolent tumor cells into chemoresistant cancer stem cells. Cancer Cell 31, 110–126 (2017). [PubMed: 27989801]

64. Evdokimova V, Tognon CE, Benatar T, Yang W, Krutikov K, Pollak M, Sorensen PHB, Seth A, IGFBP7 binds to the IGF-1 receptor and blocks its activation by insulin-like growth factors. Sci. Signal 5, ra92 (2012). [PubMed: 23250396]

65. Pen A, Moreno MJ, Durocher Y, Deb-Rinker P, Stanimirovic DB, Glioblastoma-secreted factors induce IGFBP7 and angiogenesis by modulating Smad-2-dependent TGF-β signaling. Oncogene 27, 6834–6844 (2008). [PubMed: 18711401]

66. Akaogi K, Okabe Y, Sato J, Nagashima Y, Yasumitsu H, Sugahara K, Miyazaki K, Specific accumulation of tumor-derived adhesion factor in tumor blood vessels and in capillary tube-like structures of cultured vascular endothelial cells. Proc. Natl. Acad. Sci. U.S.A 93, 8384–8389 (1996). [PubMed: 8710880]

67. Sato J, Hasegawa S, Akaogi K, Yasumitsu H, Yamada S, Sugahara K, Miyazaki K, Identification of cell-binding site of angiomodulin (AGM/TAF/Mac25) that interacts with heparan sulfates on cell surface. J. Cell. Biochem 75, 187–195 (1999). [PubMed: 10502291]

68. Sarrazin S, Lamanna WC, Esko JD, Heparan sulfate proteoglycans. Cold Spring Harb. Perspect. Biol 3, a004952 (2011). [PubMed: 21690215]

69. Ricard-Blum S, The collagen family. Cold Spring Harb. Perspect. Biol 3, a004978 (2011). [PubMed: 21421911]

70. Kao Y-C, Jiang S-J, Pan W-A, Wang K-C, Chen P-K, Wei H-J, Chen W-S, Chang B-I, Shi G-Y, Wu H-L, The epidermal growth factor-like domain of CD93 is a potent angiogenic factor. PLOS ONE 7, e51647 (2012). [PubMed: 23272129]

71. Akiel M, Guo C, Li X, Rajasekaran D, Mendoza RG, Robertson CL, Jariwala N, Yuan F, Subler MA, Windle J, Garcia DK, Lai Z, Chen H-H, Chen Y, Giashuddin S, Fisher PB, Wang X-Y, Sarkar D, IGFBP7 deletion promotes hepatocellular carcinoma. Cancer Res 77, 4014–4025 (2017). [PubMed: 28619711]

72. Norsworthy PJ, Fossati-Jimack L, Cortes-Hernandez J, Taylor PR, Bygrave AE, Thompson RD, Nourshargh S, Walport MJ, Botto M, Murine CD93 (C1qRp) contributes to the removal of apoptotic cells in vivo but is not required for C1q-mediated enhancement of phagocytosis. J. Immunol 172, 3406–3414 (2004). [PubMed: 15004139]

73. Pellicani R, Poletto E, Andreuzzi E, Paulitti A, Doliana R, Bizzotto D, Braghetta P, Colladel R, Tarticchio G, Sabatelli P, Bucciotti F, Bressan G, Iozzo RV, Colombatti A, Bonaldo P, Mongiat M, Multimerin-2 maintains vascular stability and permeability. Matrix Biol 87, 11–25 (2020). [PubMed: 31422156]

74. Tian Y, Sun Y, Gao F, Koenig MR, Sunderland A, Fujiwara Y, Torphy RJ, Chen LP, Edil BH, Schulick RD, Zhu Y, CD28H expression identifies resident memory CD8 + T cells with less cytotoxicity in human peripheral tissues and cancers. Oncoimmunology 8, e1538440 (2019). [PubMed: 30713797]

75. Khan S, Taverna F, Rohlenova K, Treps L, Geldhof V, de Rooij L, Sokol L, Pircher A, Conradi L-C, Kalucka J, Schoonjans L, Eelen G, Dewerchin M, Karakach T, Li XR, Goveia J, Carmeliet P, EndoDB: A database of endothelial cell transcriptomics data. Nucleic Acids Res 47, D736–D744 (2019). [PubMed: 30357379]

76. Zhu Y, Yao S, Iliopoulou BP, Han X, Augustine MM, Xu H, Phennicie RT, Flies SJ, Broadwater M, Ruff W, Taube JM, Zheng L, Luo L, Zhu G, Chen J, Chen L, B7-H5 costimulates human T cells via CD28H. Nat. Commun 4, 2043 (2013). [PubMed: 23784006]

77. Robinson MD, McCarthy DJ, Smyth GK, edgeR: A bioconductor package for differential expression analysis of digital gene expression data. Bioinformatics 26, 139–140 (2010). [PubMed: 19910308]

78. Tang Z, Li C, Kang B, Gao G, Li C, Zhang Z, GEPIA: A web server for cancer and normal gene expression profiling and interactive analyses. Nucleic Acids Res 45, W98–W102 (2017). [PubMed: 28407145]

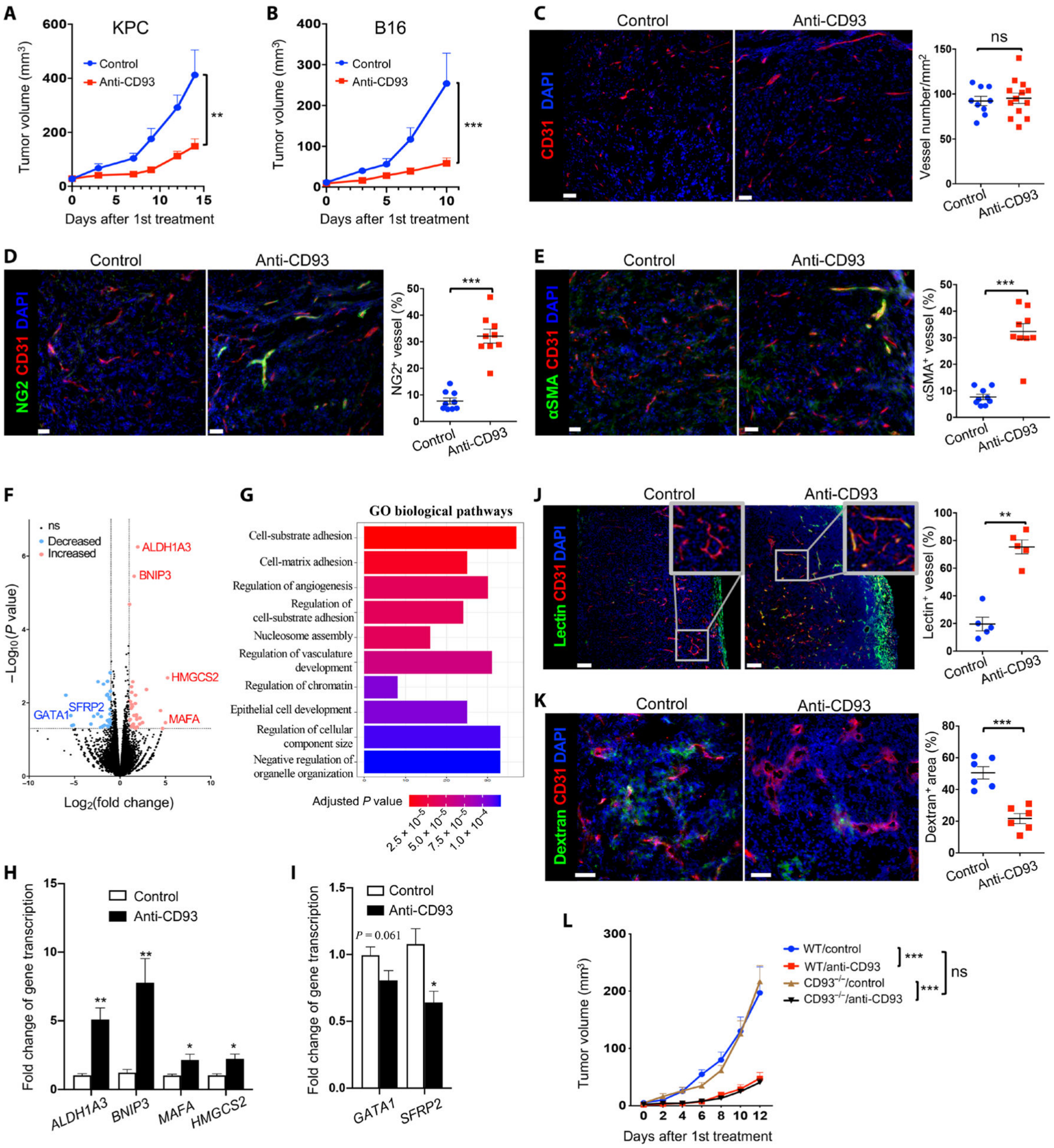

Fig. 1. Anti-CD93 inhibits tumor growth and promotes vascular maturation in mice.
(**A** and **B**) Subcutaneous KPC (A, $n = 12$) and B16 melanoma (B, $n = 10$) tumors in mice were treated with CD93 mAb (7C10) twice a week when tumors became palpable. Data are representative of at least three independent experiments. (**C** to **E**) KPC tumor tissue was obtained on day 8 after antibody treatment. Blood vessel numbers within tumors were quantified by CD31 staining (C). Images and comparisons of tissues for blood vessels (CD31) expressing NG2 (D) and αSMA (E) to assess blood vessels covered by pericytes and smooth muscle cells, respectively. Data are representative of two independent experiments. Scale bars, 50 μm. DAPI, 4′,6-diamidino-2-phenylindole. (**F** to **I**) RNA-seq was performed on ECs isolated from KPC tumors in mice. Volcano plot revealed differentially expressed genes between control- and anti-CD93–treated groups (F).

Gene ontology analysis was performed to identify biological pathways for differentially expressed genes (G). Quantitative PCR was performed to validate the expression increases of *ALDH1A3*, *BNIP3*, *MAFA*, and *HMGCS2* (H), and the decreases of *GATA1* and *SFRP2* (I). (**J** and **K**) KPC tumor-bearing mice after 1 week of antibody treatment were assessed for lectin perfusion (J) and for dextran leakage (K). Data are representative of two independent experiments. Scale bars, 50 μm. (**L**) WT B6 mice were reconstituted with bone marrow cells from WT or CD93$^{-/-}$ mice. Eight weeks after reconstitution, mice were inoculated with B16 tumor cells and started with antibody treatment. Tumor volumes were measured at the time points shown after first treatment. $n = 10$ to 13. Data are representative of two independent experiments. Data are presented as means ± SEM. Data in (A), (B), and (L) were analyzed with two-way ANOVA test. Data in (C) to (F) and (H) to (K) were analyzed with unpaired Student's t test. $^{*}P < 0.05$, $^{**}P < 0.01$, and $^{***}P < 0.001$. ns, not significant.

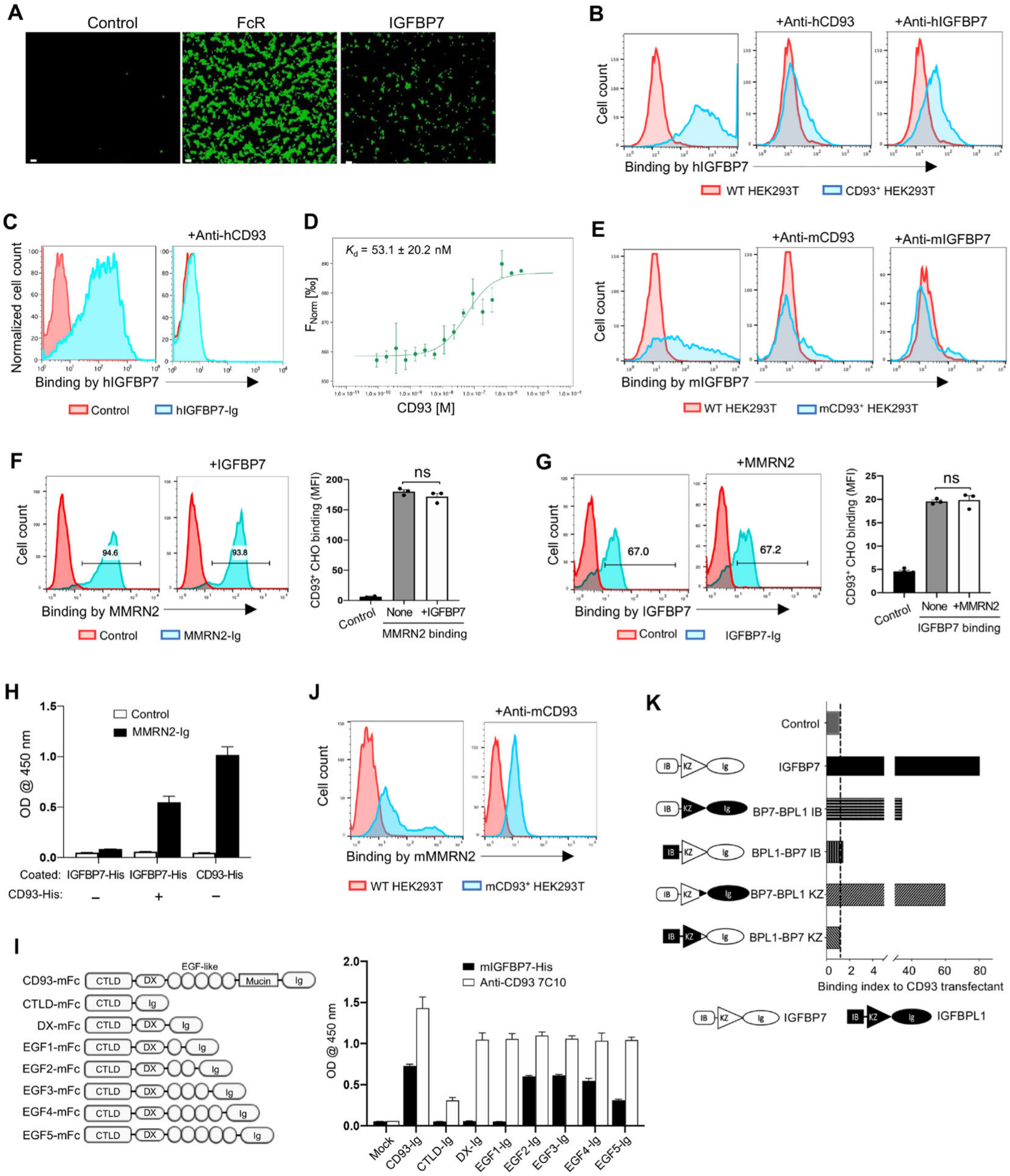

Fig. 2. IGFBP7 is identified as a binding partner for CD93.

(**A**) Graphic views of individual wells with a positive hit (IGFBP7) for CD93-Ig in a GSRA screening system. Scale bars, 50 μm. (**B**) HEK293T cells transfected with control (red) or CD93 construct (blue) were stained with IGFBP7-Ig for binding, with the presence of anti-CD93 (MM01) or anti-IGFBP7 (R003) mAb. Data are representative of two independent experiments. (**C**) HUVEC cells were stained with control (red) or IGFBP7-Ig (blue), with or without the presence of CD93 mAb (MM01). Data are representative of two independent experiments. (**D**) Microscale thermophoresis binding curve of human IGFBP7 to CD93 protein. (**E**) HEK293T cells transfected with control (red) or mouse CD93 construct (blue) were stained with mouse IGFBP7-Ig for binding, with the presence of anti-mouse CD93 (clone 7C10) or anti–mouse IGFBP7 (clone 2C6). Data are representative of at least three independent experiments. (**F**) CD93$^+$ CHO cells were stained with MMRN2-Ig, with or without the presence of IGFBP7-His protein. Data are representative of two independent experiments. MFI, mean fluorescent intensity. (**G**) CD93$^+$ CHO cells were stained for IGFBP7 binding, with or without the addition of MMRN2 protein. Data are representative of two independent experiments. (**H**) Wells coated with IGFBP7-His protein were incubated with CD93-His protein before examining for MMRN2-Ig binding by ELISA. Wells coated with CD93-His protein served as a positive control. Data are representative of two independent experiments. (**I**) Wells coated with mIGFBP7-His or anti-mCD93 (7C10) were incubated with mFc-tagged mCD93 fragment fusion proteins for binding by ELISA. Data are representative of two independent experiments. (**J**) HEK293T cells transfected with control (red) or CD93 construct (blue) were stained with MMRN2-Ig, with or without the presence of anti-mCD93 (7C10). Data are representative of two independent experiments. (**K**) Schematic diagrams represent the structure of a series of chimeric proteins that were generated by replacing each domain of IGFBP7 (BP7) with a corresponding portion from IGFBPL1 (BPL1). The binding of each chimeric protein to CD93 transfectant was tested by flow cytometry. Binding index refers to the ratio of mean fluorescence intensity of CD93 transfectant to control cells.

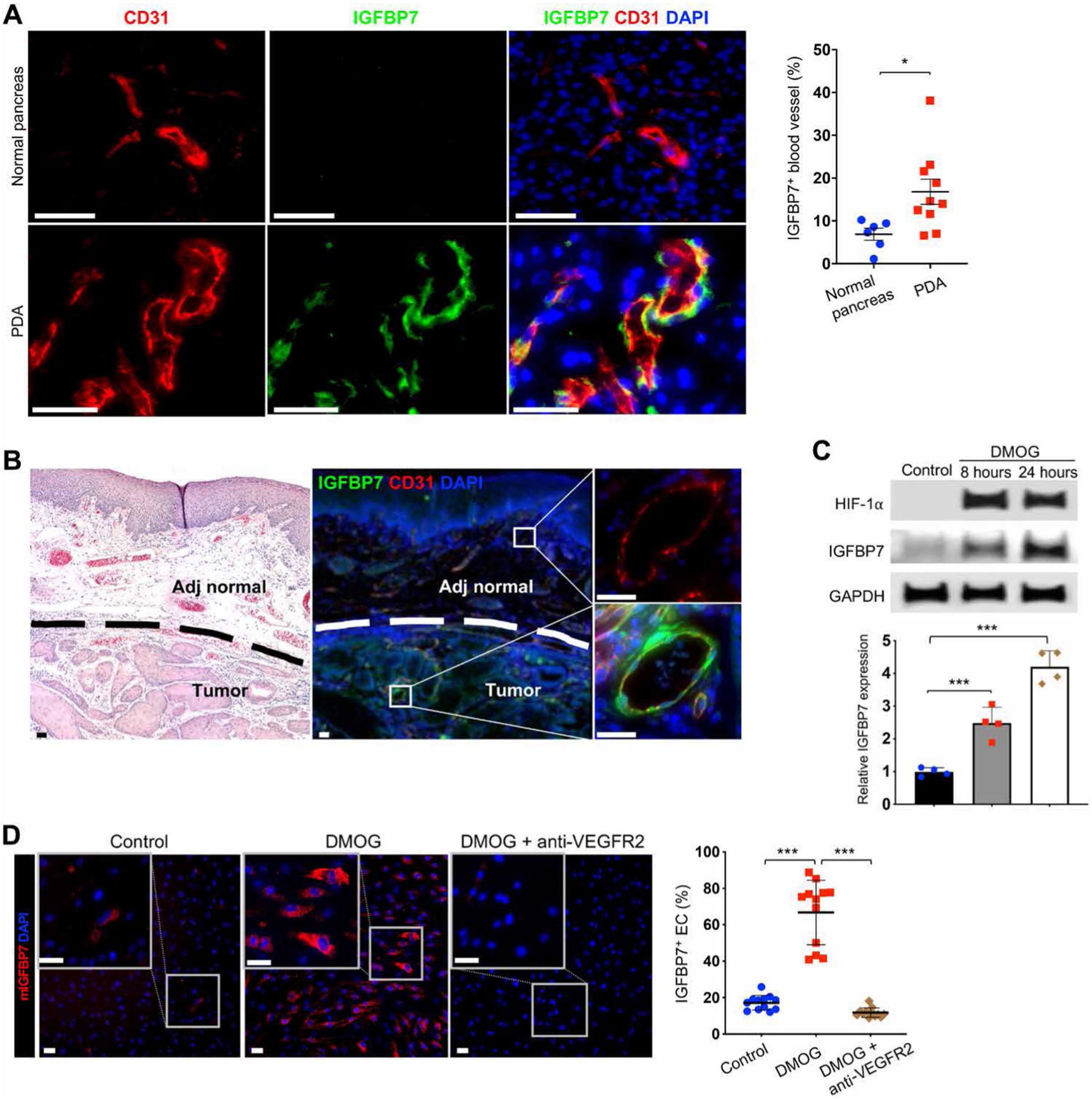

Fig. 3. IGFBP7 is up-regulated on tumor vasculature.

(**A**) IGFBP7 expression on blood vessels ($CD31^+$) in normal pancreas and PDA tissues. Each dot represents the mean value for one tissue. Scale bars, 50 μm. (**B**) Representative image of IGFBP7 expression on blood vessels ($CD31^+$) in human head and neck cancer tissue. H&E staining was performed to identify tumor from the adjacent normal tissue (Adj normal). Scale bars, 20 μm. (**C**) HUVEC cells treated with DMOG were examined for HIF-1α and IGFBP7 expression by Western blot. IGFBP7 protein was compared by densitometric quantification. Data are representative of two independent experiments. (**D**) MAECs under the treatment of DMOG with or without VEGFR2-blocking mAb for 24 hours were examined for IGFBP7 expression. Data are representative of two independent experiments. Scale bars, 20 μm. Data presented as means ± SEM. Data in (A) were analyzed with unpaired Student’s *t* test. Data in (C) and (D) were analyzed with one-way ANOVA test with a Tukey post hoc test. $^*P < 0.05$ and $^{***}P < 0.001$.

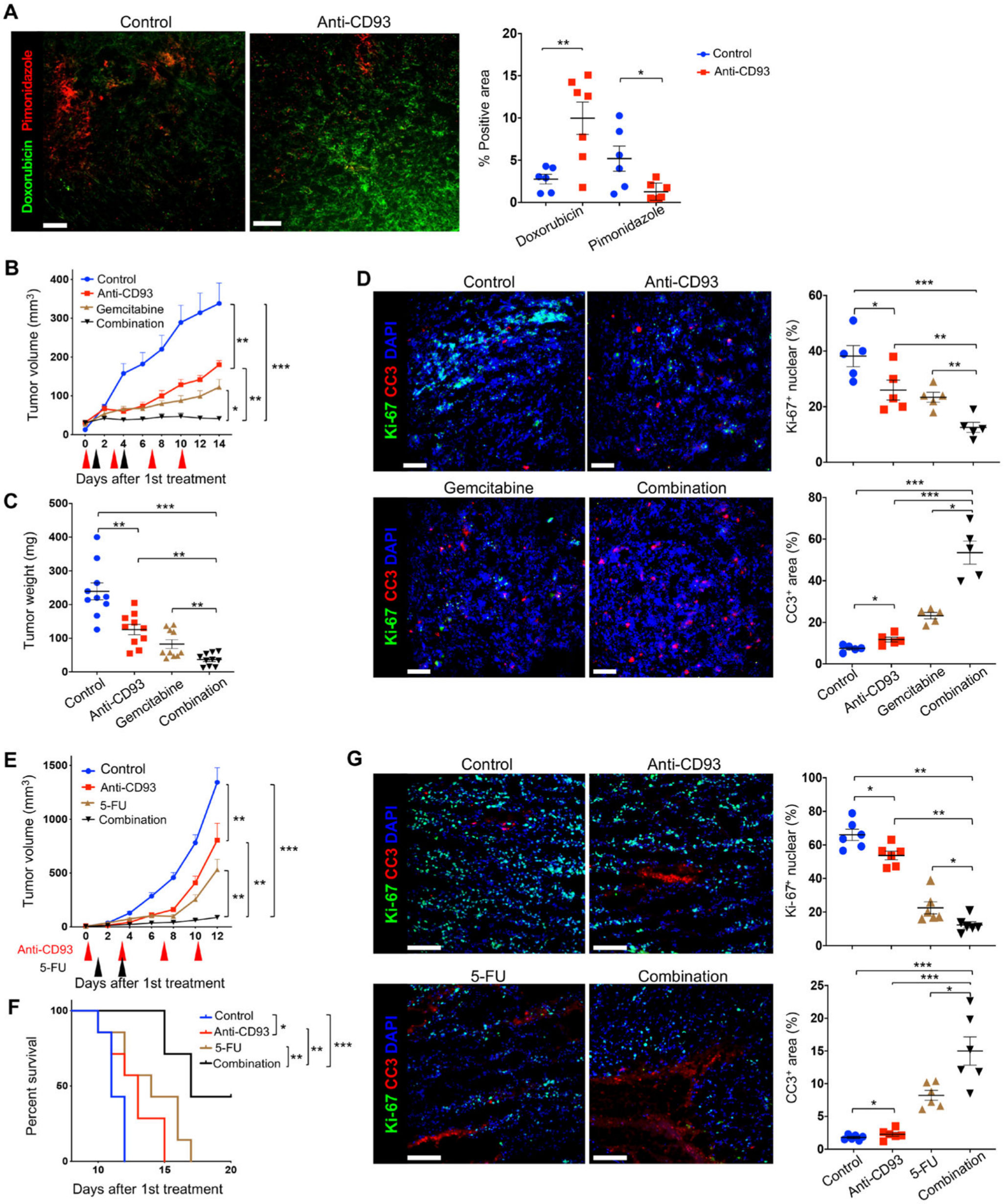

Fig. 4. Anti-CD93 treatment improves drug delivery and facilitates chemotherapy.

(**A**) KPC tumor-bearing mice under antibody treatment for 8 days were injected with doxorubicin and pimonidazole for the assessment of drug delivery and hypoxia, respectively. Data are representative of two independent experiments. Scale bars, 50 μm. (**B** to **D**) KPC tumor-bearing mice were treated with antibody (red arrowhead) and/or gemcitabine (black arrowhead). Tumor growth (B) and tumor weight at day 14 (C) are shown. *n* = 10. Tumor tissues harvested on day 14 after therapy were stained for Ki-67 and cleaved caspase 3 (CC3) (D). Scale bars, 50 μm. Data are representative of two independent experiments. (**E** to **G**) B16 tumor-bearing mice were treated with antibody (red arrowhead) and/or 5-FU (black arrowhead). Tumor growth (E, *n* = 10) and survival curve (F, *n* = 7) of groups with different treatments are shown. Tumor tissues harvested on day 14 after therapy were stained for Ki-67 and CC3 (G). Scale bars, 50 μm. Data are representative of two independent experiments. Data presented as means ± SEM. (A) analyzed with unpaired Student's *t* test. Data in (B) and (E) analyzed with two-way ANOVA test with a Dunnett's post hoc test. (F) Kaplan-Meier curves analyzed with log-rank (Mantel-Cox) test. Data in (C), (D), and (G) analyzed with one-way ANOVA test with a Tukey post hoc test. *$P < 0.05$, **$P < 0.01$ and ***$P < 0.001$.

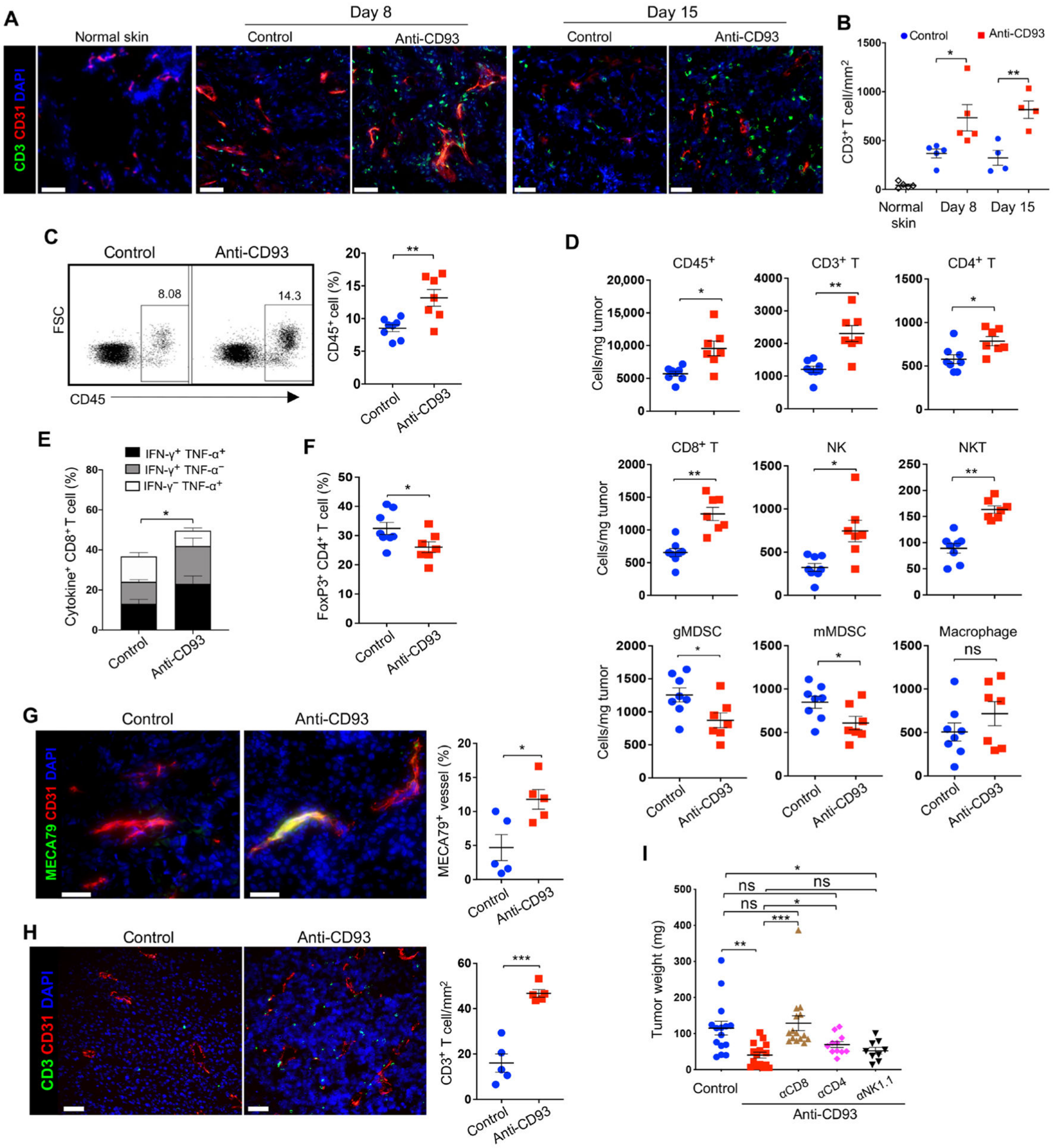

Fig. 5. CD93 blockade promotes immune cell infiltration to inhibit tumor progression.

(**A** and **B**) Representative images (A) and quantifications (B) of CD3$^+$ T cells (green) in healthy skin of naive mice and implanted KPC tumors harvested on days 8 and 15 after antibody treatment. Scale bars, 50 μm. Data are representative of three independent experiments. (**C** to **F**) Single-cell suspensions were prepared from KPC tumors harvested on day 8 after antibody therapy. Flow cytometry analysis was performed to determine the percentage of infiltrating CD45$^+$ leukocytes (C) and the densities of different immune cells (D). The percentages of effector cytokine-producing CD8$^+$ T cells (E) and Foxp3$^+$ T$_{reg}$ in CD4$^+$ T cells (F) were quantified. Data are representative of two independent experiments. (**G**) Images and comparisons of MECA79 expression (green) on CD31$^+$ blood vessels (red) within KPC tumors harvested on 8 days after antibody treatment. Data are representative to two independent experiments. Scale bars, 50 µm. (**H**) Images and comparisons of CD3$^+$ T cells (green) within subcutaneous B16 tumors 14 days after antibody treatment. Scale bars, 50 µm. Data are representative of two independent experiments. (**I**) KPC tumor (subcutaneous model) weights after 14 days of antibody treatment were determined. In some mice, CD8$^+$ T cells, CD4$^+$ T cells, or NK (including NKT) cells were eliminated by a corresponding depleting antibody. Data are representative of two independent experiments. Data presented as means ± SEM. Data in (B) and (I) were analyzed with one-way ANOVA test with a Tukey post hoc test. Data in (C) to (H) were analyzed with unpaired Student's *t* test. $^*P < 0.05$, $^{**}P < 0.01$, and $^{***}P < 0.001$.

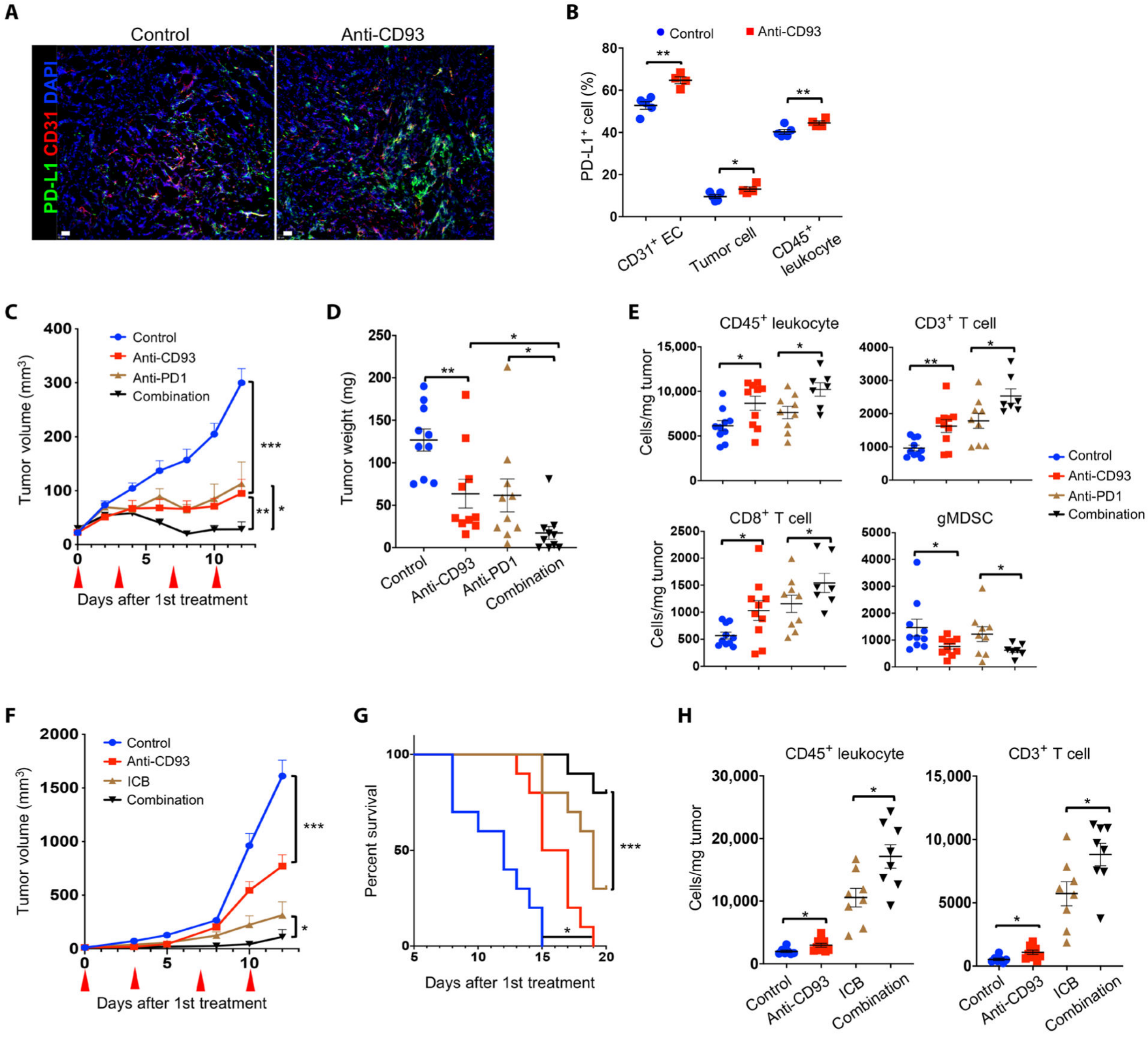

Fig. 6. CD93 blockade sensitizes tumors to ICB therapy.

(**A** and **B**) Representative images of PD-L1 expression (green) in subcutaneous KPC tumors harvested on day 15 after antibody treatment. Scale bars, 50 μm. Single-cell suspensions prepared from KPC tumor tissues were quantified for PD-L1 expression by flow cytometry. (**C** to **E**) B6 mice with palpable KPC tumors were divided into four groups and treated with control, anti-CD93, anti-PD1, or the combination of anti-CD93 and anti-PD1 at the time points indicated by the red arrowheads. Tumor growth curve (C) and tumor weight 12 days after treatment (D) were measured. *n* = 10. The densities of respective immune cells within tumors were determined by flow cytometry (E). Data are representative of two independent experiments. (**F** to **H**) Mice with palpable B16 tumors were treated with control, anti-CD93, ICB (PD1 + CTLA mAbs), or the combination of anti-CD93 and ICB at the time points indicated by the red arrows. Tumor growth (F) and survival curve (G) of groups were shown. *n* = 10. The densities of CD45$^+$ leukocytes and CD3$^+$ T cells within tumors harvested on day 12 were determined by flow cytometry (H). Data are representative of two independent experiments. Data presented as means ± SEM. Data in (B) analyzed with unpaired Student’s *t* test. Data in (D), (E), and (H) analyzed with one-way ANOVA test with a Tukey post hoc test. Data in (C) and (F) analyzed with two-way ANOVA test with a Dunnett's post hoc test. (G) Kaplan-Meier curves analyzed with log-rank (Mantel-Cox) test. $^*P < 0.05$, $^{**}P < 0.01$, and $^{***}P < 0.001$.